Plasma properties conditioned by the magnetic throat location in a helicon plasma device

Alfio E Vinci, Stéphane Mazouffre

Journal of Applied Physics

Plasma properties conditioned by the magnetic throat location in a Helicon plasma device

Alfio E Vinci[a] and Stéphane Mazouffre[b]
Institut de Combustion, Aérothermique, Réactivité et Environnement (ICARE), Centre National de la Recherche Scientifique, 1C Avenue de la Recherche Scientifique, 45071 Orléans, France

(Dated: 21 September 2021)

Measurements are conducted in a Helicon plasma device to analyze the spatial distribution of plasma properties as the throat of the magnetic nozzle is axially shifted with respect to the antenna center. Krypton plasma is generated in the sub-kilowatt range and probed using a suite of diagnostics including a rf-compensated Langmuir probe, a planar probe and laser-induced fluorescence. It is found that larger ion currents and increased plasma confinement are achieved when the throat of the magnetic nozzle is located downstream the antenna center, at a distance that equals or exceeds two times the antenna length. The ions, although being accelerated, retain subsonic velocities even beyond the magnetic throat.

I. INTRODUCTION

A recent keen interest in electric space propulsion stems from an increasing number of small satellites being deployed for plural applications[1–6]. Simple and compact thrusters can allow for in-space maneuvering of such small spacecrafts[7] which usually do not boast large volume capacity to meet the needs of consolidated technologies, e.g. Gridded Ion thrusters and Hall thrusters. As a result, a portion of research and development efforts are being focused on electrodeless devices and magnetic nozzle (MN) acceleration[8–13]. This kind of technology can indeed offer a number of advantages compared to the aforementioned state-of-the-art devices. Issues linked to erosion of components are expected to be of little consequence due to the absence of direct interaction between plasma discharge and electrodes, resulting in a long lifetime. The plasma beam leaving the discharge chamber is quasineutral, thus no neutralizer is required. Furthermore, these plasma sources can more easily operate using condensible propellants with respect to those system that require a dedicated neutralizer, whose lifetime and reliable functioning can be considerably affected[14].

The Helicon plasma (HP) thruster is one such a device. It mainly comprises three components: *i*) a dielectric tube as plasma discharge region, *ii*) a radiofrequency (rf) antenna for gas ionization and *iii*) an axially directed steady magnetic field for plasma confinement and expansion throughout its diverging region, i.e. the magnetic nozzle. Power radiated by the antenna is deposited in the electron population as thermal energy by means of helicon wave modes[15] and Trivelpiece–Gould wave modes[16]. The energy is used for plasma production and transport phenomena, such as ambipolar electric field, resulting in axial acceleration of the ions in the MN by conversion of the electron thermal energy.

The maturity of this technology is still relatively low[5], whereby several undesired aspects come along with the considered advantages. The most critical one perhaps regards the thrust efficiency. Thus far, direct thrust measurements have revealed efficiencies typically below 10 % in many different devices[13,17–24], with the only recent exception of nearly 20 % at several kW of input power[12]. In this scenario, improving the attained performance is required in order to turn HP thrusters into a competitive technology in the near future. The better understanding of the physics governing such rf plasma sources by exploring the different working parameters is currently the preferred approach to provide an exhaustive optimization pathway.

In an effort to model HP discharges, previous analyses have considered different magnetic topologies inside the source tube, e.g. uniform[25,26], Helmholtz and Maxwell configurations[27]. The magnetic field inside the source is then matched with a divergent geometry through a magnetic throat localized in the proximity of the tube exit. This firm condition is not necessarily the most convenient solution, as demonstrated in Ref. 28 where a stepped-diameter tube is employed and the magnetic throat is placed downstream the exit cross section of the small main tube. Besides, virtually every numerical and experimental work studying the influence of magnetic nozzle on the plasma properties, limited the analysis to the exploitation of different magnitudes at the throat. A fruitful investigation is reported in Ref. 29, where the location of the magnetic throat is indirectly shifted with respect to the antenna − which is constantly located at the back plate − by changing the discharge tube length. Another relevant analysis is reported in Ref. 30, where the authors characterized the plasma and the rf power circuit when the magnetic throat localized either within the source or at the exhaust. Bennet *et al.*[31] studied the generation of plasma as a function of the MN throat location. Yet, their setup did not include plasma expansion outside the discharge tube and many operating conditions relied on magnetized ions, which is not a typical scenario in propulsion. The shape of the magnetic nozzle and the location of the throat are presumably strongly linked to the amount of the input energy that can be usefully converted into axial thrust. Energetic electrons are mainly produced close to the region occupied by the antenna. Several phenomena occur in the nozzle, such as transport due to pressure gradient and electron cooling via convection and/or conduction, which determine the conversion efficiency of inlet thermal energy into

[a]alfio.vinci@cnrs-orleans.fr
[b]stephane.mazouffre@cnrs-orleans.fr

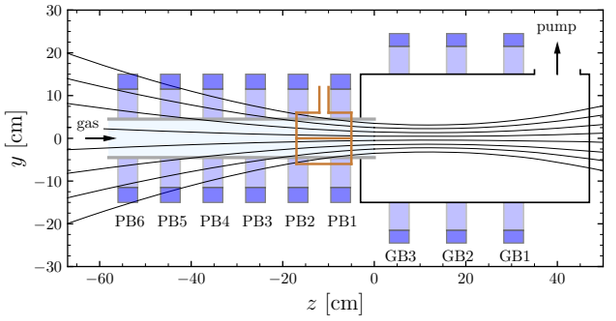

FIG. 1. Helicon source schematics. The $z = 0$ position refers to the discharge tube outlet, $y = 0$ refers to the reactor axis.

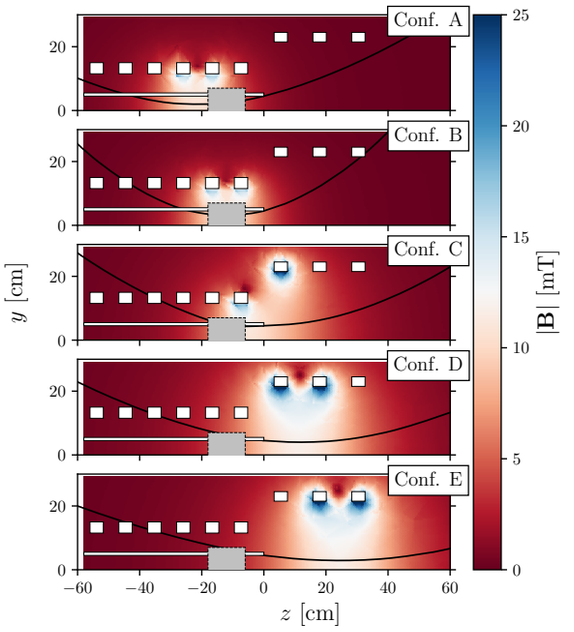

FIG. 2. 2D profiles of the externally applied magnetic fields. White line indicates the discharge tube walls, white rectangles represent the magnetic coils, the gray rectangle indicates the antenna region and the black solid line exemplifies the magnetic streamline crossing the tube edge at $z = 0$.

ion acceleration. Furthermore, as the throat is shifted along the thruster axis with respect to the antenna location, the expansion ratio of the plasma beam changes, thus resulting in possibly different thrust levels.

This paper reports on experimental results obtained in a HP source operating with krypton under several configurations of the external magnetic field. Numerous plasma properties are spatially resolved as the throat of the magnetic field is moved with respect to the antenna axial position. A detailed description of the experimental setup is provided in Section II, including the HP source and the magnetic configurations. In Section III, the diagnostics are extensively described. They include: a rf-compensated Langmuir probe to spatially characterize plasma density, electron temperature, and plasma potential; a planar probe to measure the ion current density; laser-induced fluoresce to explore the axial ions and atoms velocity distribution function. Measurements are presented and discussed in Section IV. Eventually, conclusions are drawn in Section V.

II. EXPERIMENTAL SETUP

A schematics of the HP source employed in this study is shown in Figure 1 along with an example of computed magnetic field lines. The entire experimental setup is oriented in a vertical position.

The discharge chamber consists in a borosilicate glass tube with $\phi = 9$ cm inner diameter and $L = 58$ cm length, whose open exit arbitrarily identifies the origin of the axial coordinate z. Krypton gas is introduced off-axis in the tube through its top aperture at a nominal flow rate of 1 ± 0.004 mg s^{-1}. The bottom part is connected to a 30 cm in inner diameter and 50 cm in length expansion chamber made in aluminum which is equipped with a turbomolecular/primary pumping system. The ultimate base pressure is in the order of 10^{-5} mbar, whereas the typical pressure during operation reads $\sim 5 \times 10^{-3}$ mbar.

The rf antenna in use is a double-saddle type with $d_A = 12$ cm length centered at $z \cong -11$ cm. It is made of pure copper and features two feeding arms which are long enough to be directly connected to the matching network so that power losses due to intermediate links are prevented. Input rf power is generated by a 1 kW-class power supply at 13.56 MHz and kept constant to 750 W throughout the reported measurements. The power carried by higher order harmonics is certified to be lower than -40 dBc. Matching of the rf power is attained via a custom π-type network. During operation, values of the reflected power are below ~ 2 %.

A set of nine electromagnets surrounds both the discharge tube and the expansion chamber. Their denomination is reported in Figure 1. Each electromagnet is made up of a 2 mm diameter copper wire, constituting 510 loops for PB1-6 and 430 loops for GB1-3. The presence of multiple electromagnets enables the investigation of profoundly different magnetic field topologies. For the purpose of this study, five magnetic configurations are examined by powering two electromagnets at once. In doing so, the location of the magnetic throat is intentionally relocated along the z axis. The tested magnetic configurations are progressively labeled as Conf. A to Conf. E. When involved, PB coils are powered with 3 A and GB coils with 6 A of direct current. Figure 2 shows the computed 2D magnetic field maps, highlighting the streamline that crosses the discharge tube edge at $z = 0$, thus defining the ideal shape of the plasma plume (whether it is assumed fully magnetized). With reference to Figure 2, it is noteworthy to emphasize on the magnetic throat location. It moves from upstream the antenna in Conf. A to far downstream the an-

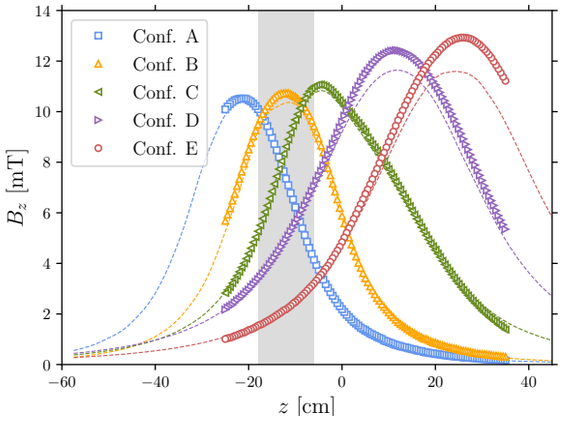

FIG. 3. Externally applied magnetic field on-axis profiles. Shaded area indicates the antenna location. Dashed lines represent simulation profiles, scatter points indicate probe measurements.

tenna in Conf. E. The first axial mode the antenna can generate translates in an axial wavelength as $\lambda_z = 24$ cm, see Section IV C. Notice that the magnetic throat in Conf. D is approximately one wavelength downstream of the antenna center. The magnitude of the on-axis magnetic field is reported in Figure 3 by comparing computed values and measured values. All magnetic configurations feature a peak value of $10 \div 13$ mT with a similar qualitative profile but shifted along z.

III. DIAGNOSTICS

A. RF-compensated Langmuir probe

Plasma density n_p, electron temperature T_e and plasma potential V_p are measured using a rf-compensated Langmuir probe (LP), see Figure 4. A detailed description of the probe has been previously reported in[11]. It is designed in accordance with the results reported in[32–34]. A tungsten wire of 0.38 mm in diameter and 5 mm in length constitutes the probe tip. An additional electrode made of stainless steel contributes to rf compensation and provides mechanical support to the assembly. The electrode is electrically insulated from the probe tip using a 1 mm in outer diameter alumina tube. A 1 nF axial capacitor is soldered to the compensation electrode and connected in parallel with the probe tip and a series of three axial chokes, each of which self-resonates at one of the first three harmonics. The whole assembly is encapsulated inside a borosilicate glass tube of 6 mm outer diameter, which also accommodates the coaxial cable for probe biasing and current

FIG. 4. RF-compensated Langmuir probe.

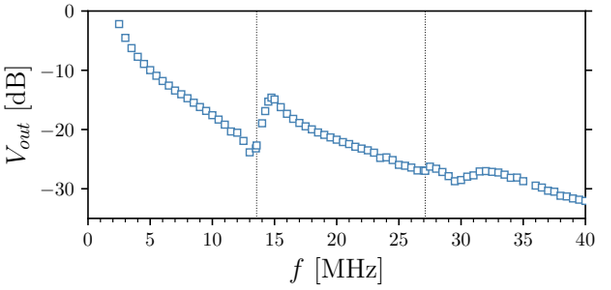

FIG. 5. RF-compensated LP frequency spectrum ($V_{ref} = 10$ V). Vertical dotted lines indicate 13.56 MHz and 27.12 MHz.

measuring.

Chokes selection is attained by characterization of their impedance frequency spectrum. A 20 V_{pp} sinewave is generated by a function generator and fed to one lead of the testing choke. The other lead is connected to a 46.52 kΩ resistor and the series circuit closes to the ground. The frequency of the input sinewave is swept while the voltage drop across the resistor is monitored and used to calculate the current flowing in the circuit. The frequency at which the current is minimum is the choke self-resonating frequency. Functional check of the whole probe assembly is performed by applying a 20 V_{pp} sinewave to the tungsten tip at different frequencies. The probe output is recorded by a digital oscilloscope and shown in Figure 5 as a function of the input frequency. Local minima are evident in correspondence of the harmonic frequencies, as desired.

The probe is manually displaced within the plasma using a single-axis translation stage with a resolution of 10 µm and a stroke of 150 mm. Probe alignment is ensured by the use of a cross-line laser pendulum. I-V curves are recorded using a ALP control unit by Impedans Ltd. Thereafter, data is post-processed relying on OML theory[34,35]. Assuming local quasineutrality, plasma density n_p is inferred from the linear fit of the ion current squared versus the probe potential. The ion current fit is then subtracted from the total current to obtain a better estimation of the electron current. Assuming the electrons are described by a Maxwell-Boltzmann distribution function, the logarithmic profile of the electron current is linearly fitted, enabling the estimation of the electron temperature T_e. The plasma potential V_p is computed as the probe bias voltage where the first derivative of the I-V curve features its peak value.

Uncertainty associated with the probe measurements is estimated through a statistical approach. The detailed procedure has been previously reported in[11]. The outline of the analysis shows that all plasma parameters are measured with a statistical deviation as high as ~ 2 %.

B. Planar probe with guard ring

The ion current density j_i is measured using a planar probe with a guard ring (PPGR). It mainly comprises a disk-shaped

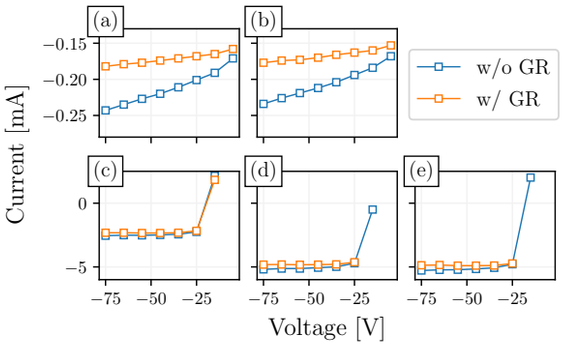

FIG. 6. Ion current profiles at $(x, y = 0; z = 15$ cm). Subplots denomination is linked to magnetic configurations Conf.s A-E.

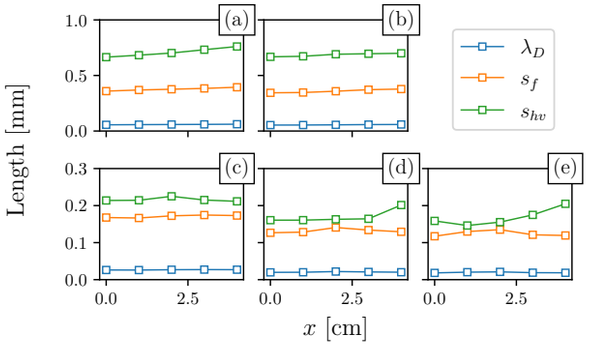

FIG. 7. Debye length, floating and high-voltage sheath thickness at $z = 15$ cm. Subplots denomination is linked to magnetic configurations Conf.s A-E.

collector and an outer ring, both made in stainless steel. The role of the guard ring is to concentrate sheath edge effects far from the collector, thus ensuring that the ion collection area exactly corresponds to the collector geometrical area[36]. For correct functioning of the probe, it is required that *i*) the width of the guard ring is much larger than the local plasma sheath thickness and *ii*) the gap between the two electrodes is smaller than the local sheath thickness to introduce negligible potential irregularities. The collector is 5.6 mm in diameter and 1 mm in thickness, whereas the ring width is 1 mm. A gap of 100 µm is maintained between the two electrodes to ensure electrical insulation. Each electrode features a separated electrical connection for polarization and current measurement. Voltage is applied to the collector by way of a Keithley 2410 SourceMeter, which is also used to measure the flowing current. The guard ring is biased using a TTIEX752M power supply.

Functional check of the probe is carried out by recording the I-V curves at $(x, y = 0; z = 15$ cm) for the five magnetic configurations denominated Conf.s A-E. The curves obtained with a biased and floating guard ring are compared in Figure 6. Saturation of the ion current is achieved for Conf.s C-D-E at voltages lower than about -40 V, while no complete saturation is recorded for Conf.s A and B due to the fact that the guard ring width is not compatible with the local values of the sheath thickness. This can be confirmed by computing the local values of the characteristic lengths over the radial coordinate using the values of n_p and T_e later discussed in Section IV. Floating and high voltage sheath thickness, s_f and s_{hv} respectively, are computed in accordance with[37], using -75 V for Conf.s A-B and -50 V for Conf.s C-D-E. Outcomes are plotted in Figure 7. It results evident that values of s_{hv} for Conf.s C-D-E are much smaller than the guard ring width, whereas those for Conf.s A and B approach its size. It shall be noted that the attainment of a perfectly flat profile of the ion saturation current would require a guard ring width $5 \div 10$ times larger than the actual one. Thus, the overall probe size would probably lead to serious plasma perturbations. Furthermore, the scope of the presented measurements is not to, e.g., focus on indirect propulsive performance estimation but rather to perform a more qualitative-like comparison of the five magnetic configurations.

Given the high level of reproducibility recorded during preliminary measurements, the uncertainty in j_i is mainly given by the uncertainty in the measured current and the probe collecting area. This consideration leads to a value of < 8 %.

The planar probe is manually actuated from outside the chamber using the single-axis translation stage described in Section III A.

C. Laser-induced fluorescence setup

Ions and atoms velocity distribution functions (VDFs) are measured by means of laser-induced fluorescence (LIF) spectroscopy. The technique and the optical bench in use have been extensively described in previous works[38,39]. Excitation of metastable levels is achieved via an amplified tunable single-mode laser diode in the $810 - 840$ nm spectral range. The primary laser beam is split in multiple beams with the purpose of *i*) instantaneous monitoring of the laser mode and detection of any mode hop by means of a Fabry-Pérot interferometer, *ii*) laser power check using a photodiode and *iii*) accurate wavelength measurement by way of a calibrated wavemeter whose absolute uncertainty is $\sim 60\,\mathrm{m\,s^{-1}}$ (80 MHz). Modulation of the laser beam is achieved using a mechanical chopper at ~ 1.9 kHz. The laser is coupled to a 50 µm optical fiber which allows transporting the laser beam from the optical bench to the Helicon source setup. Laser is injected inside the vacuum chamber through a borosilicate glass window located

TABLE I. Kr I and Kr II probed optical transitions.

	Transition	λ_{exc} [nm] (vacuum)	λ_{fluo} [nm] (air)
Kr I	$5s^2[3/2]^\circ_1 \rightarrow 5p^2[3/2]_2$	819.23095	760.15457
Kr II	$5p^2D^\circ_{5/2} \rightarrow 5s^2P_{3/2}$	820.4959	461.91658

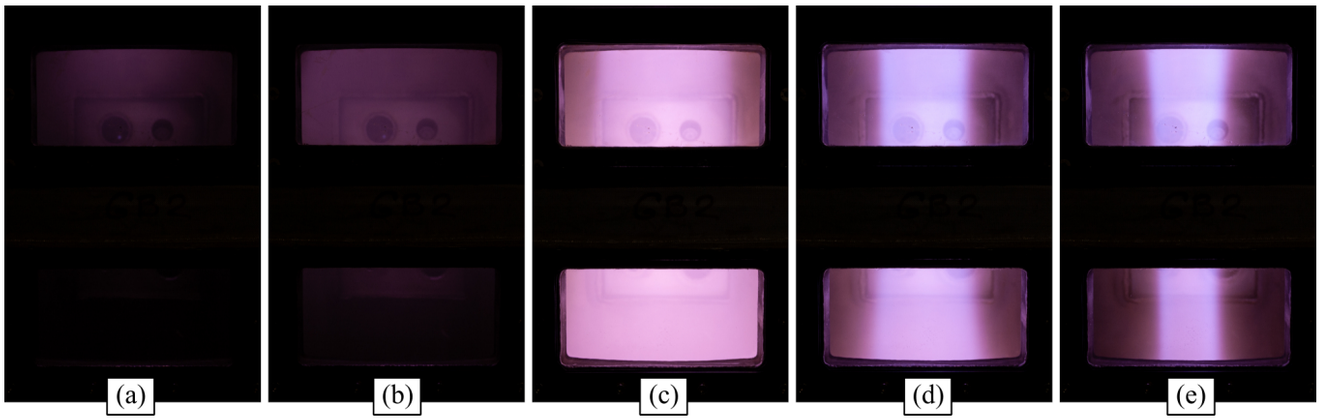

FIG. 8. Photographs of the plasma plume in (a) Conf. A, (b) Conf. B, (c) Conf. C, (d) Conf. D and (e) Conf. E. Windows are centered at $z = 12$ and $z = 24$ cm.

at the bottom of the reactor. Note that $\mathbf{k}\cdot\mathbf{v} < 0$ here, where $\mathbf{k}$ is the laser wavenumber and $\mathbf{v}$ the particle velocity. The laser beam is collimated using a combination of a 150 mm and a 1000 mm focal length plano-convex lenses. Uncertainty on the alignment with respect to the HP source axis is estimated to be $\lesssim 1.6$ deg. In order to ensure a linear regime of the studied optical transitions, the laser power density delivered to the plasma is kept below $1.2\,\mathrm{W\,mm^{-2}}$, a threshold value that has been determined during preliminary measurements. A detection branch is placed perpendicularly to the excitation beam featuring a pair of plano-convex lenses (250 mm and 100 mm focal lengths) focusing on a 200 µm core diameter optical fiber. Both the excitation and detection branches are mounted on a dedicated computer-controlled high precision linear translation stage to enable spatially resolved measurements along the y axis. The detection optical train can be additionally displaced along the z axis within a few centimeters using a manual stage. The 200 µm optical fiber transports the fluorescence light to a monochromator which isolates the desired line from the whole spectrum. Afterwards, a photomultiplier tube is used to convert the light signal into voltage, which is fed into a lock-in amplifier operating at the laser modulation frequency to distinguish the signal from the natural plasma emission. The VDFs are inferred by scanning over the laser wavelength λ and computing the particles axial velocity v_z as $v_z = c(\lambda - \lambda_0)/\lambda_0$, where λ_0 is the unshifted transition wavelength and c is the speed of light. The measured LIF profiles result from the Doppler broaden line. The presence of Kr isotopes leads to broadening due to isotopic shift and hyperfine structure[38]. Moreover, due to the presence of a steady magnetic field, the Zeeman effect splits the spectral lines into sub-levels[38]. Nevertheless, since the spectrum is dominated by the ^{84}Kr isotope and the magnetic field is relatively weak, it is herein assumed that the observed fluorescence line profile images the local VDF.

The probed optical transitions are reported in Table I. The zero-velocity wavelength for Kr I is estimated from preliminary measurements in the HP source shining the laser along the x axis. The other listed wavelengths are given in the literature[38–42].

IV. EXPERIMENTAL RESULTS AND DISCUSSION

A. Visual inspection

The very first piece of information regarding the way the plasma responds to the applied magnetic field topology is provided by visual inspection. The photographs of the plasma plume reported in Figure 8 are taken using a common DSLR camera framing the region $8 < z < 28$ cm and set at f/8 and $1/40$ s exposure time. It results evident how significant differences characterize the extracted plasma plume when employing the different magnetic topologies. A faint plume is visible when the reactor operates in Conf. A and Conf. B. Instead, a well defined plasma beam is noticed when Conf.s C, D and E are chosen. In the latter cases, the plasma radius visibly delineates the local magnetic streamlines, cf. Figure2 and Figure8. It is interesting to notice that the local magnitude of the axial component B_z is nearly equal for Conf. C and Conf. E at $z = 12$ cm (see Figure2), i.e. at the center of the top window in Figure8. Yet, the two plasma beams show a very different structure. As a matter of fact, local values of the field radial component B_r and gradient $\partial B_z/\partial z$ significantly differ. This finding agrees with previous numerical models[26,43] and intrinsically points out that both $|\mathbf{B}|$ and $\nabla\mathbf{B}$ have an impact on the plasma behavior.

B. LP measurements

Plasma properties are characterized using the diagnostics described in Section III. The region delimited by $0 < y < 4$ cm and $-4 < z < 21$ cm is probed by means of the rf-compensated LP. I-V characteristics are recorded with a spatial resolution of 5 mm. Data is post-processed as discussed in Section III A and eventually interpolated to enhance visualization. Figures 9, 10 and 11 illustrate normalized 2D maps of n_p, T_e and V_p, respectively, for the five magnetic topologies. Normalization values are: 6×10^{17} m^{-3} as regards to n_p, 6 eV for T_e and 25 V for V_p. The solid black lines

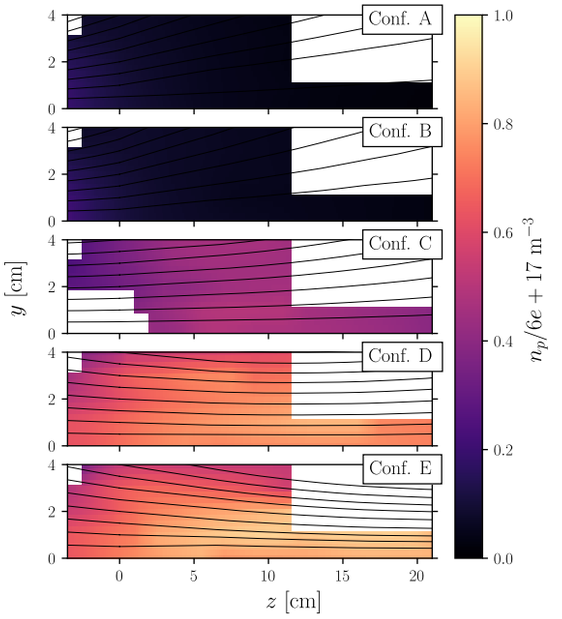

FIG. 9. Normalized plasma density for the five magnetic configurations. Normalization factor is 6×10^{17} m^{-3}. Solid black lines represent magnetic streamlines.

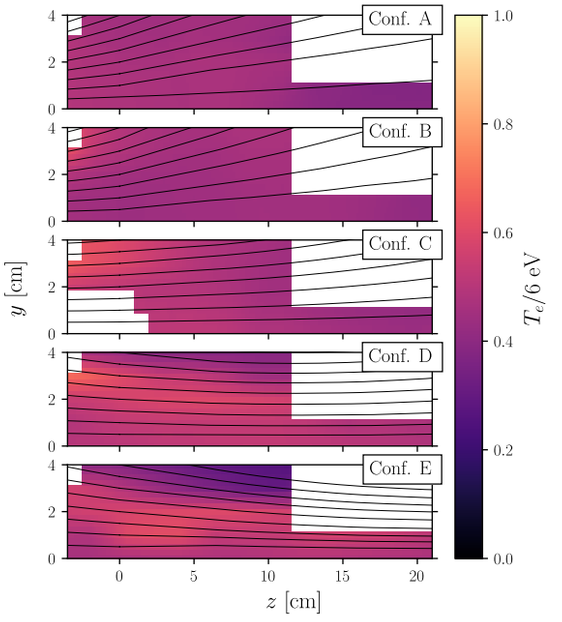

FIG. 10. Normalized electron temperature for the five magnetic configurations. Normalization factor is 6 eV. Solid black lines represent magnetic streamlines.

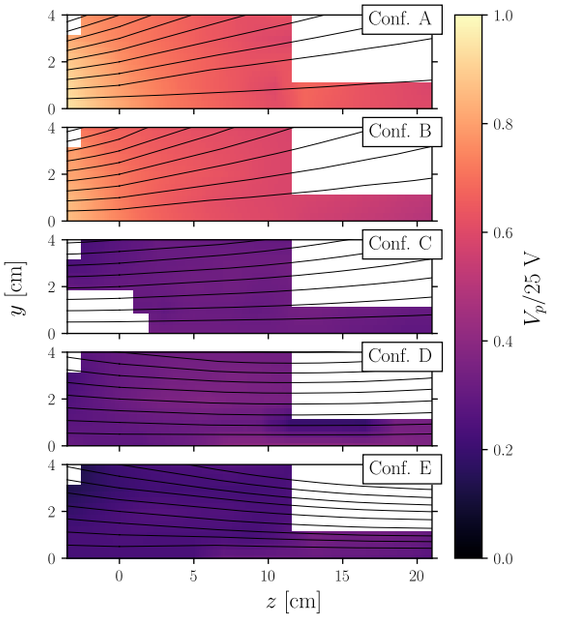

FIG. 11. Normalized plasma potential for the five magnetic configurations. Normalization factor is 25 V. Solid black lines represent magnetic streamlines.

included in the figures represent the magnetic streamlines delimited by the discharge tube edge at $z = 0$. Furthermore, on-axis profiles of n_p, T_e and V_p are shown in Figure 12. These experimental measurements show that:

1. when the HP source operates in Conf. A, the extracted plasma plume is characterized by a low monotonically decreasing profile of n_p ranging between $\sim 1 \times 10^{17}$ and $\sim 9 \times 10^{15}$ m^{-3} along the reactor axis. The profile of T_e features a monotonic behavior as well, with a peak value of ~ 3 eV. In a similar fashion, V_p drops from ~ 24 V to ~ 15 V. All plasma properties peak on-axis at $z < 0$. These quantitative observations agree with the faint light emitted in the nozzle region, as stated beforehand. Visual check of the plasma also reveals that light is instead concentrated within the discharge tube. It suggests that the radial and back boundaries represent a major loss term of plasma[26,44].

2. when the HP source operates in Conf. B, analogous arguments can be put forward. The profile of n_p likewise peaks on-axis at $z < 0$ and decays monotonically downstream. Altogether, slightly larger values of n_p are measured with respect to Conf. A. In the bulk of the plasma, T_e remains in the order of ~ 3 eV with lower values downstream. However, a population of relatively more energetic electrons ($T_e \sim 3.5$ eV) appears off-axis, in correspondence of the magnetic nozzle edge, visible at $z < 0$ in Figure 10(b). Although qualitatively very

similar, the distribution of V_p for Conf. B presents lower values with respect to Conf. A of a few volts.

3. when the HP source operates in Conf. C, results similar to those previously reported in[11] using the same HP source are obtained. As a matter of fact, in both the experiments the magnetic throat is located at $z = 0$. In contrast to what was discussed in points (i) and (ii), all plasma properties peak off-axis. Data acquisition in the region $(0 < r < 2, z < 0)$ was not possible due to discharge instability possibly induced by the probe presence. The largest value of n_p is recorded at $z > 0$ and it reads $\sim 3 \times 10^{17}$ m^{-3}, whereas T_e reaches a peak of 4 eV at $z < 0$. The distribution of V_p is relatively isotropic, ranging in the 8 ± 0.5 V interval. The reason why n_p and T_e present separated regions of the respective maximum values has been explained in[11,45] in terms of pressure balance. When considering the z component of the electron momentum conservation equation in the limit of negligible contribution due to momentum transfer collisions and due to the Lorenz force, the potential gradient and the pressure gradient balance each other. In the region where $B_r/B_z \ll 1$, i.e. where the local magnetic field divergence angle is small, the reduced cross field electron mobility yields a relatively large axial conductivity, resulting in a nearly null potential gradient. Hence, for equilibrium reasons, the pressure gradient is required to be small, which results in a larger n_p where T_e is lower and vice versa. Similar results are numerically found and discussed in[46].

4. when the HP source operates in Conf. D, light emission upstream the antenna is almost absent, hinting that plasma losses at the back and lateral walls are mitigated with respect to the previous cases. With reference to Figure 9(d), it is evident that n_p follows the axial gradient of B_z. The maximum value of $\sim 5 \times 10^{17}$ m^{-3} is therefore located in correspondence of the magnetic throat. In Figure 10(d), it is relevant to notice the distinct transport pattern of a relatively more energetic electron population along the magnetic field lines at the edge of the nozzle, which exhibits $T_e \approx 3.5 \div 4.2$ eV. A relatively small V_p is measured throughout the probed region, with a peak value in the order of 10 V in the area of maximum n_p.

5. when the HP source operates in Conf. E, similar observations to those stated in point (4) can be raised. Profiles of n_p and T_e have a strong dependence on the spatial distribution of B_r and B_z. The highest plasma density value among all the studied magnetic configurations is herein recorded to be $\sim 5.5 \times 10^{17}$ m^{-3} nearby the magnetic throat. As highlighted in point (4), also in this case a more energetic population of electrons is transported along the external surface of the magnetic nozzle, cf. Figure 10(e). At $z \cong 10$ cm, all the electrons with $T_e \gtrsim 3$ eV are concentrated in a radius of about 3 cm, as visually confirmed by Figure 8(e).

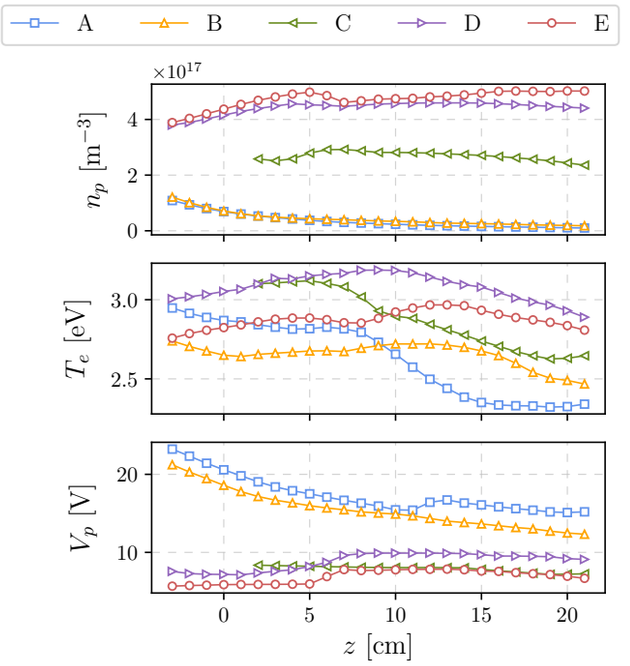

FIG. 12. On-axis profiles of (top) plasma density, (middle) electron temperature and (bottom) plasma potential. Data is extracted from Figures 9-11 and down-sampled to enhance visualization.

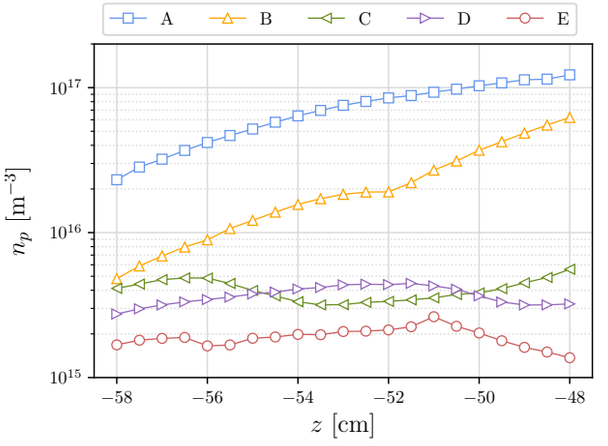

FIG. 13. Ion density profile in the proximity of the back-plate for the five magnetic configurations.

Eventually, it is worth observing that the different configurations of B possibly influence the power deposition map. This, in turn, very likely relates to the different spatial distributions of n_p and T_e as discussed in points (1)-(5).

In addition to the measurements performed using the rf-compensated LP, a simple uncompensated LP is inserted on-axis at the back/injection plate of the HP source to measure n_p as an indicator of the plasma flux lost in this region. The probe is biased to scan over the ion saturation branch only.

No significant distortions due to rf oscillations are expected in this part of the I-V curve[33]. For obtaining this particular set of data, the reactor injection plate has been modified in order to accommodate the probe and its related wiring. The propellant is still injected off-axis but it goes through a plenum first and eventually reaches the discharge tube via a multi-perforated surface, resulting in a axial gas flow. An uncompensated probe is chosen due to limitations on the available room. The measured profiles of n_p are shown in Figure 13 for Conf. A to E. Since the magnetic throat in Conf. A is located upstream the antenna, the ions are mostly transported towards the back plate by following the convergent-divergent shape of the magnetic field. As the magnetic throat moves farther downstream from the antenna center, lower densities are measured in the proximity of the injection plate, as expected.

C. Plasma density profile model

Using a simplified description of the plasma, the measured axial profiles of n_p can be compared with theoretical profiles retrieved from the helicon wave dispersion relation, which is thereafter derived accounting for the non-uniformity of the external magnetic field along z. This approach implicitly assumes that the plasma production entirely relies on the wave-mode power coupling. Although the helicon regime is not proven here by direct measurement of the excited wave, previous experiments performed on the same device operated with similar ranges of magnetic field strength and input power have shown the presence of the propagating wave[11]. Considering that the electric $\tilde{\mathbf{E}}$ and magnetic $\tilde{\mathbf{B}}$ components of the exited wave are described[47,48] as

$$\tilde{\mathbf{E}}, \tilde{\mathbf{B}} \sim \exp[i(m\theta + k_z z - \omega t)], \tag{1}$$

where m is the azimuthal mode number, θ is the azimuthal angle and k_z is the axial wavenumber, Maxwell equations assume the form

$$\nabla \cdot \tilde{\mathbf{B}} = 0, \tag{2a}$$

$$\nabla \times \tilde{\mathbf{E}} = i\omega\tilde{\mathbf{B}}, \tag{2b}$$

$$\nabla \times \tilde{\mathbf{B}} = \mu_0 \mathbf{j}. \tag{2c}$$

The electron momentum equation is written as

$$-en_p\tilde{\mathbf{E}} = i\frac{m_e}{e}\mathbf{j}_e(\omega + i\nu) - \mathbf{j}_e \times \mathbf{B}, \tag{3}$$

where $\mathbf{j}_e$ is the electron current density, $\mathbf{B}$ is the external magnetic field and ν is a collision rate accounting for all dissipation phenomena. Additional comments and derivation of Equation 3 are reported in[47]. The widespread ideal assumption of perfectly uniform magnetic field is not appropriate in the actual case. Therefore, although still simplistic, it is assumed that $\mathbf{B} = B(z)\hat{\mathbf{z}}$, i.e. only the variation of the magnetic field along z is accounted for. Combining Equation 2a-(2c) and Equation 3, one obtains

$$\left(\frac{\omega + i\nu}{\omega_{c_e}}\right)\nabla \times (\nabla \times \tilde{\mathbf{B}}) \quad + k_z \nabla \times \tilde{\mathbf{B}} + \\ + \frac{\mu_0 \omega e n_p}{B}\tilde{\mathbf{B}} = \mathbf{0}, \tag{4}$$

where the explicit dependence on z has been omitted, ω_{c_e} is the electron cyclotron frequency and the rest is conventional. Detailed derivation of Equation 4 is likewise included in[47]. Eventually, in the limit of $m_e \to 0$, the local dispersion relation is retrieved in the same shape of the well known 0D dispersion relation, i.e.

$$k(z)k_z = \frac{\mu_0 \omega e n_p(z)}{B(z)}, \tag{5}$$

where $k(z)$ indicates the total wavenumber. The wave boundary conditions are fixed by[48]

$$mk(z)\mathrm{J}_m[k_r(z)r_p(z)] + k_z \mathrm{J'}_m[k_r(z)r_p(z)] = 0, \tag{6}$$

where J_m and $\mathrm{J'}_m$ are the Bessel function of the first kind of order m and its derivative, respectively, $k_r(z)$ is the local radial wavenumber and $r_p(z)$ is the local plasma radius. The value of k_z is fixed by the antenna length, i.e. $k_z = \pi/d_A, 3\pi/d_A, 5\pi/d_A$, etc. Pretending that only the first order axial mode is coupled with the antenna, the computation algorithm includes:

- the axial wavenumber is estimated as $k_z = \pi/d_A$, therefore the axial wavelenth is $\lambda_z = 24$ cm;
- $r_p(z)$ is set equal to the radius of the magnetic streamline crossing the tube edge at $z = 0$, see Figure 2;
- considering the geometry of the antenna and the direction of the external magnetic field, it is imposed that $m = +1$;
- two cases are distinguished:
  1. $k_r(z)$ is computed numerically from Equation 6 and it is named as $\kappa_1(z)$ for the sake of clarity in the following;
  2. $k_r(z)$ is evaluated as $\kappa_1(z)\sin[\alpha(z)]$ referred to as $\kappa_2(z)$ hereafter. Here $\alpha(z)$ is the local magnetic field divergence angle. The purpose of this heuristic strategy is to provide the model with the information that the applied magnetic field is not

TABLE II. Helicon wave parameters at $z = 10$ cm.

	Conf. A	Conf. B	Conf. C	Conf. D	Conf. E
r_p [cm]	7.3	8.1	5.1	4.0	3.5
k_z [cm^{-1}]	0.26	0.26	0.26	0.26	0.26
λ_z [cm]	24	24	24	24	24
κ_1 [cm^{-1}]	0.46	0.41	0.68	0.88	1.03
κ_2 [cm^{-1}]	0.14	0.17	0.07	-0.01	-0.08

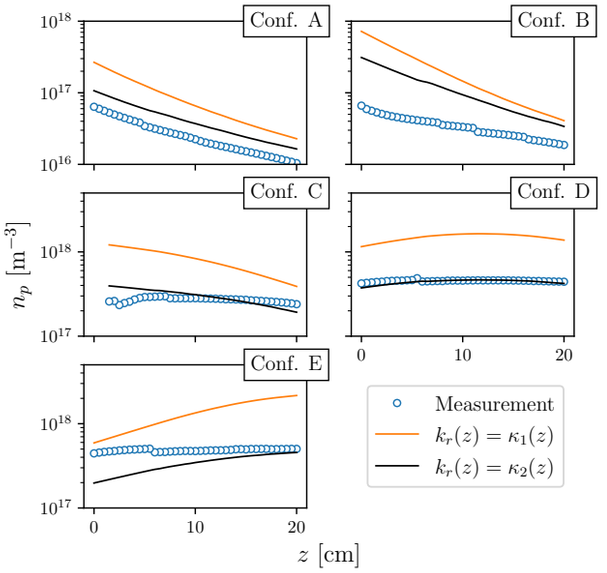

FIG. 14. Plasma density at $r = 0$ computed using the helicon waves dispersion relation in the $k_r(z) = \kappa_1(z)$ and $k_r(z) = \kappa_2(z)$ cases compared to measurement data.

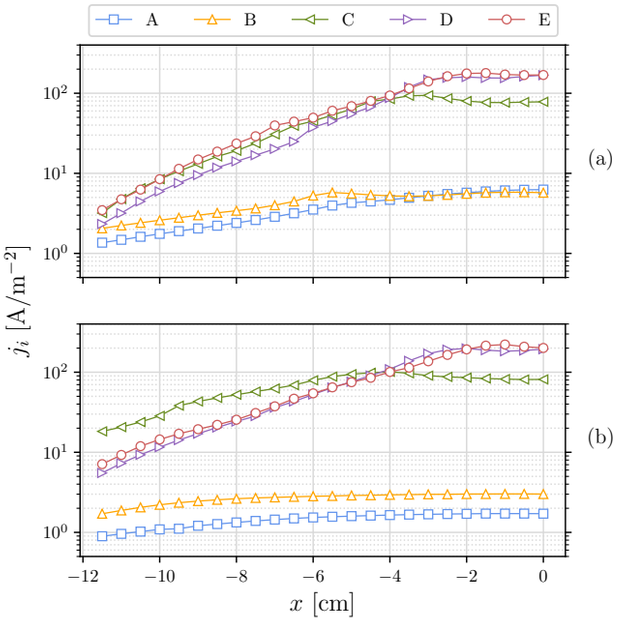

FIG. 15. Ion current density at (a) $z = 5$ and (b) $z = 15$ cm for the five magnetic configurations.

purely axial. In doing so, it is postulated that the helicon wave resonance cone reduces to a line at the magnetic throat, i.e. where $\alpha = 0$, thus k equals k_z.

- the profile $n_p(z)$ is consequently computed from Equation 5 for the aforementioned two cases.

Numerical values of the relevant parameters are reported in Table II for all magnetic configurations. In Figure 14, the obtained theoretical curves are compared with measurements of n_p extracted from Figure 9 at $x, y = 0$ for all the tested magnetic configurations. In general, it is found that the case $k_r(z) = \kappa_1(z)$ provides an overestimation of the plasma density. When dealing with Conf.s D and E, the $k_r(z) = \kappa_2(z)$ case is in very good agreement with the data in correspondence of the magnetic throat, that is where the strong assumption $\mathbf{B} = B(z)\hat{\mathbf{z}}$ is more representative. Ultimately, n_p measured in Conf. C is in relatively good agreement with the latter case. It is noted that even the $k_r(z) = \kappa_2(z)$ case overestimates the measured values of n_p for Conf.s A and B, although matching the qualitative profile. This suggests that the helicon wave is evanescent in this region of the plasma since the measured n_p is lower than the one required by the dispersion relation. In conclusion, these profiles of n_p computed from the dispersion relation represent a first effective estimation of the actual spatial evolution of plasma density. Therefore, these quantitative information can be of some convenience for guessing the propagation region of helicon waves and for preliminary modeling of the plasma dynamics and/or design of the axial magnetic field profile.

TABLE III. Plume divergence parameter δ from data in Figure 15.

	Conf. A	Conf. B	Conf. C	Conf. D	Conf. E
δ at $z = 5$ cm	0.218	0.359	0.041	0.014	0.021
δ at $z = 15$ cm	0.523	0.567	0.224	0.028	0.035

D. PPGR measurements

A further insight into the properties of the plasma when operating with the different magnetic topologies is rendered by the employment of the PPGR described in Section III. The probe is displaced radially along the x axis at $z = 5$ cm and $z = 15$ cm in order to analyze the divergence of the extracted plasma plume. The measurements of j_i are shown in Figure 15(a-b). Table III gathers the values of the divergence parameter δ computed as the ratio $j_i(x = -11.5\text{ cm})/j_i(x = 0\text{ cm})$. Results confirm that a low-current high-divergence ion beam is extracted from the HP source when operating in Conf. A and B. Differently, the ion beams related to Conf.s C, D and E feature a similar low-divergence profile of j_i in the proximity of the tube exit, see Figure 15(a). Yet, the divergence angle of Conf. C rapidly grows as the plasma expands downstream, cf. Figure 15(b). The highest value of j_i is recorded in Conf.E at $z = 15$ cm, in agreement with the largest n_p probed in the same configuration. Larger values of j_i relate well with higher propellant utilization efficiency, which is a desirable working condition for space propulsion applications.

TABLE IV. Order of magnitude of relevant velocity quantities.

	$\mathcal{O}(v)$
Ion acoustic velocity	$v_B = \sqrt{kT_e/m_i} \approx 2000\ \mathrm{m\,s^{-1}}$
Thermal velocity	$v_{th} = \sqrt{8kT_i/\pi m_i} \approx 275\ \mathrm{m\,s^{-1}}$

E. LIF measurements

Using LIF spectroscopy, the velocity distribution functions of krypton atoms Kr I and ions Kr II are inferred. Information about the velocity of the ions is of particular interest for driving conclusions about propulsive performance. On the other hand, knowledge of the atoms velocity is useful for modeling of the plasma flow. Table IV exemplifies the order of magnitude of the relevant velocity terms in the HP source operating with Kr. Radial profiles of Kr I VDF are evaluated at $z = 12$ cm and shown in Figure 16 for all magnetic configurations. The spatial resolution is 10 mm. In this case, the reported data did not require any post-processing as a adequate signal-to-noise ratio was found. These measurements show that the most probable velocity of Kr I is nearly unchanged over the different magnetic topologies, reading $\sim 250 \div 300\ \mathrm{m\,s^{-1}}$, therefore in the order of the thermal velocity assuming $T_i \approx 300$ K, cf. Table IV. No dependence of the velocity on the radial location y is recorded. Dissimilar values of velocity spread are found between the magnetic configurations, with a broader VDF for Conf. C and Conf. D.

Axial VDFs of Kr II are probed in the same radial region with a spatial resolution of 5 mm at three distinct axial positions, i.e. $z = 10.5$ cm, $z = 12$ cm and $z = 25$ cm. At some y locations, the LIF signal was not distinguishable from the background noise due to small local values of n_p, therefore mapping of the VDFs was not possible. For the very same reason, Conf.s A and B did not allow obtaining an appropriate signal-to-noise ratio in any of the probed locations. Raw VDFs are post-processed using a least squares Gaussian fit. The resulting profiles when the HP source operates in Conf.s C, D and E are reported in Figure 17, 18 and 19, respectively. In addition, the most probable velocity is extracted and plot in Figure 20 thus to facilitate comparison among the various magnetic configurations. It is noticed that the profiles related to Conf.s C and D feature a nearly identical trend, whereas the ion velocity in Conf. E generally retains lower readings. This is in agreement with the measured values of V_p which remain below those concerning Conf. C and D, cf. Figure 11. In the further upstream regions, namely $z = 10.5$ cm and $z = 12$ cm, velocities smaller than $\sim 250\ \mathrm{m\,s^{-1}}$ are measured, therefore in the order of the thermal velocity assuming $T_i \approx 300$ K. Conversely, at $z = 25$ cm, all the velocities increase by a factor of 2 to 3, reaching values as high as $\sim 500\ \mathrm{m\,s^{-1}}$. These small velocities somewhat concur with the fact that the magnetic field is weakly divergent in the probed region for Conf.s C and D, while $z = 25$ cm represents the throat location for Conf. E. A weakly divergent magnetic field does not allow for a significant momentum gain imparted by the Lorentz force. Measurements farther downstream were prevented due to the limited size of the vacuum chamber. Similar small values of ion velocity are reported in Ref. 49 using LIF on a large scale HP source. In all of the magnetic configurations, the drop of V_p is fairly small (in the order of 1 V) within $z < 21$ cm, cf. Figure 11. Considering Conf. E for instance, since at $z < 25$ cm the magnetic field is convergent, it is expected that the favored inward transport of electrons do not allow for a significant potential drop in this region. In the purely electrostatic case,

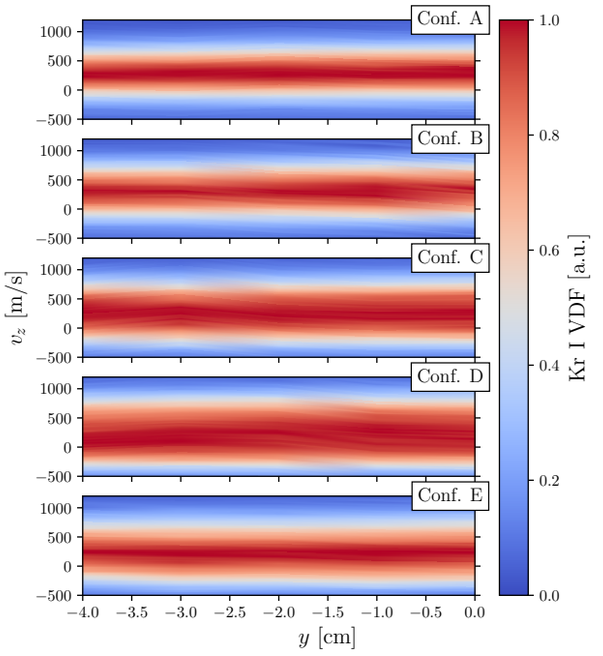

FIG. 16. Kr I velocity distribution function for the five magnetic configurations measured along the y axis at $z = 12$ cm.

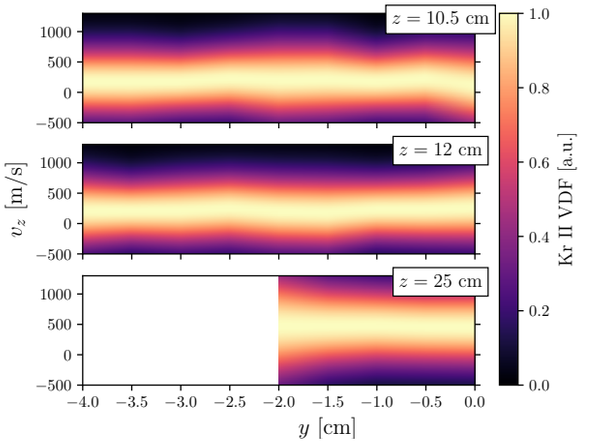

FIG. 17. Kr II velocity distribution function for Conf. C measured along the y axis at $z = 10.5$, 12 and 25 cm.

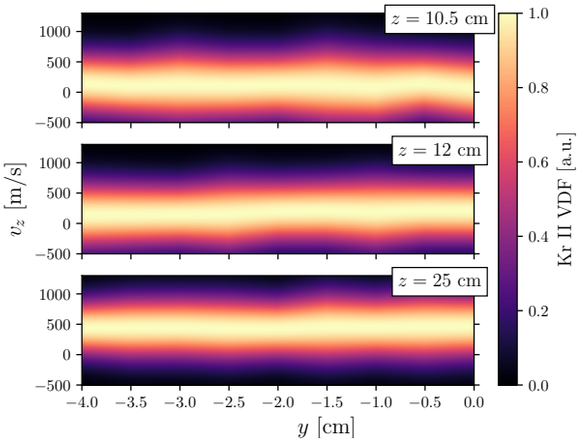

FIG. 18. Kr II velocity distribution function for Conf. D measured along the y axis at $z = 10.5$, 12 and 25 cm.

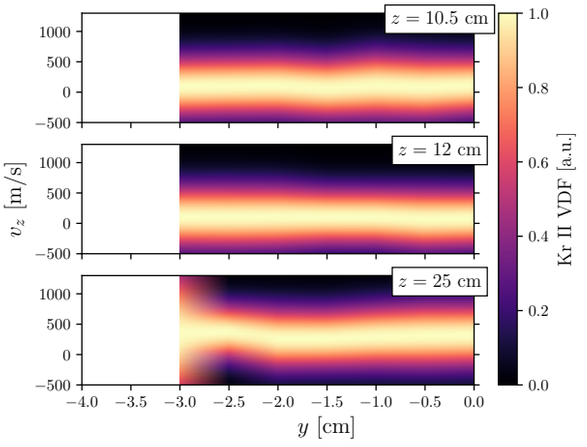

FIG. 19. Kr II velocity distribution function for Conf. E measured along the y axis at $z = 10.5$, 12 and 25 cm.

a potential drop of ~ 1 V translates into an ion velocity increase of $\sim 1.5\,\mathrm{km\,s^{-1}}$. Hence, the acceleration of the ions throughout the MN does not fully exploit the available energy. This phenomenon is related to some dissipation phenomenon, e.g. collisions, as later discussed. Moreover, although no sonic condition is achieved at the magnetic throat in Conf.s C and D, ions experience a further acceleration in the divergent part of the nozzle, see Figure 20. It suggests that the sonic point, if ever reached, is shifted downstream, in contrast with the ideal postulation of gas-dynamics-like plasma expansion[50]. In this experiment, the ions might reach the sonic speed only at the sheath edge that forms downstream between the chamber wall and the plasma plume. Numerous works focusing on modeling of magnetic nozzle dynamics have assumed that the ion Mach number equals unity at the throat[51–53]. Albeit this condition conveniently allows separating the processes of plasma generation and plasma acceleration, it is not representative in this case as well as in some other plasma beams[24,54]. Collard *et al*[24] have examined a list of phenomena which are potentially responsible for separation of the magnetic throat and the sonic point, namely electron-neutral collisions, charge-exchange collisions and ionization within the plume. In the device herein analyzed, a combination of several dissipative phenomena is likely to contribute in introducing a drag force term that prevents the ions to reach the sonic speed. In Conf. C, for instance, a significant level of ionization is localized in the near-field plume downstream the magnetic throat, as previously noted when commenting on Figure 9. This suggests that the energy stored in the electrons is spent for ions generation rather than acceleration.

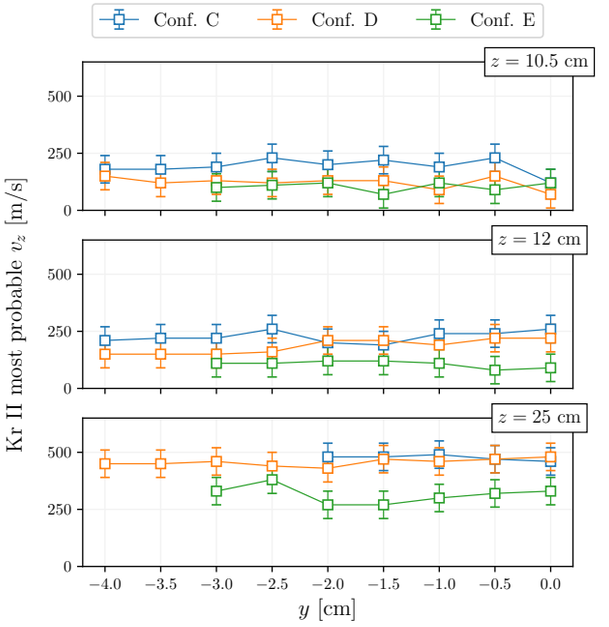

FIG. 20. Kr II most probable axial velocity extracted from Figure 17-19. Error bar is $60\,\mathrm{m\,s^{-1}}$ (typical instrument absolute error).

A parametric evaluation of the Kr II axial VDF is additionally performed at $z = 25$ cm for the purpose of better grasping the mechanisms occurring within the nozzle. The exploited parameters are: input power (750 W and 900 W); mass flow rate ($0.5\,\mathrm{mg\,s^{-1}}$, $1\,\mathrm{mg\,s^{-1}}$ and $2\,\mathrm{mg\,s^{-1}}$); current in the electromagnets (6 A and 8 A). The magnetic configuration is fixed to Conf. D for this experiment because of its divergent shape at $z = 25$ cm and larger signal-to-noise ratio with respect to Conf. C. The resulting VDFs are shown in Figure 21, which includes the raw data, the Gaussian fittings and the unfold most probable velocities obtained at each working condition. The overall tendency results clear. Indeed, higher ion velocities are attained as the mass flow rate decreases and the magnetic field is increased, whereas slower ions are recorded with larger mass flow rates. These outcomes suggest that collisions resulting from a larger pressure do play a role in the acceleration process. At lower pressures, a larger mean free path is expected, therefore allowing for greater values of T_e.

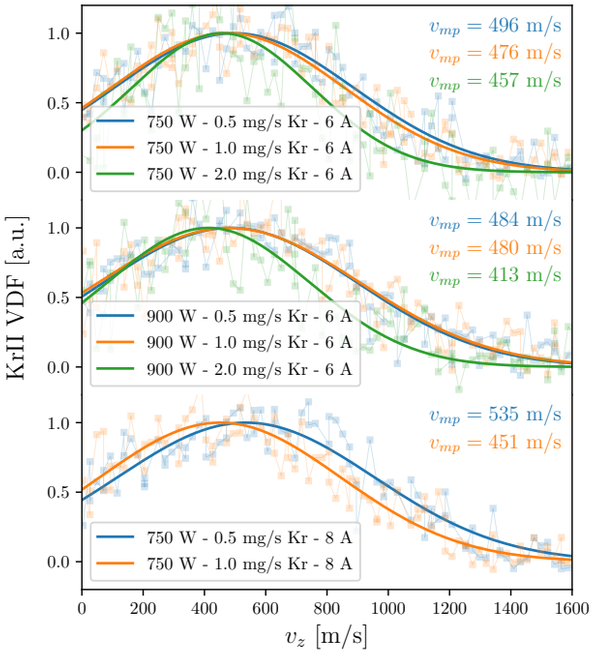

FIG. 21. Kr II axial VDF for Conf. D at $z = 25$ cm as function of P_{IN}, $\dot{m}$ and electromagnets current. Scatter points indicate raw data, solid lines exemplify least squares Gaussian fittings.

V. CONCLUSION

In summary, several plasma properties are inferred via direct measurement to establish empirical approaches to thruster design and optimization. The magnetic throat is displaced along the reactor axis and the resultant plasma is studied in the near-field plume using electrostatic diagnostics and LIF spectroscopy. It is found that a low-current high-divergence plume is extracted from the plasma source when the magnetic throat is located upstream or in correspondence of the antenna center point. Plasma density measurements at the back plate emphasize that, in those cases, the generated plasma mainly remains within the discharge tube and is lost at the radial and back boundaries. Larger ion currents and higher confinement levels are attained when the magnetic throat is located downstream the antenna, namely at a distance at least equal to the wavelength corresponding to the first order axial mode of the helicon wave. Hence, optimization of the plasma generation process in a Helicon thruster would include the separation of the magnetic throat from the antenna location in accordance with the excited helicon wavelength.

Theoretical axial profiles for the plasma density are directly derived from the dispersion relation under the hypothesis of non-uniform magnetic field. Comparison with probe measurements show relatively good agreement therefore hinting the applicability of this theoretical description for guessing the helicon wave propagation region. Furthermore, preliminary modeling and design of Helicon thrusters can perhaps make use of this approach to shape the axial magnetic field profile.

The measured ion axial velocities exhibit small values, being below the sonic condition at the magnetic throat. By measuring the most probable ion velocity obtained under different working parameters (input power, magnetic strength and mass flow rate), it is concluded that ionization and collisions occurring in the near-field plume contribute to limiting the ion acceleration process.

ACKNOWLEDGMENTS

This project has received funding from the European Union's Horizon 2020 research and innovation program under grant agreement No 870542 (HelIcon PlasmA Thruster for In-space Applications).

CONFLICT OF INTEREST

The authors have no conflicts to disclose.

DATA AVAILABILITY

The data that support the findings of this study are available from the corresponding author upon reasonable request.

REFERENCES

[1]Igor Levchenko, Kateryna Bazaka, Yongjie Ding, Yevgeny Raitses, Stéphane Mazouffre, Torsten Henning, Peter J. Klar, Shunjiro Shinohara, Jochen Schein, Laurent Garrigues, Minkwan Kim, Dan Lev, Francesco Taccogna, Rod W. Boswell, Christine Charles, Hiroyuki Koizumi, Yan Shen, Carsten Scharlemann, Michael Keidar, and Shuyan Xu. Space micropropulsion systems for Cubesats and small satellites: From proximate targets to furthermost frontiers. *Applied Physics Reviews*, 5(1), 2018.

[2]Javier Martínez Martínez, Dmytro Rafalskyi, and Ane Aanesland. Development and Testing of the NPT30-I2 Iodine Ion Thruster. In *36th International Electric Propulsion Conference*, 2019.

[3]Antonio Gurciullo, Julien Jarrige, Paul Lascombes, and Denis Packan. Experimental performance and plume characterisation of a miniaturised 50W Hall thruster. In *36th International Electric Propulsion Conference*, 2019.

[4]I. Levchenko, S. Xu, S. Mazouffre, D. Lev, D. Pedrini, D. Goebel, L. Garrigues, F. Taccogna, and K. Bazaka. Perspectives, frontiers, and new horizons for plasma-based space electric propulsion. *Physics of Plasmas*, 27(2), 2020.

[5]E. Dale, B. Jorns, and A. Gallimore. Future Directions for Electric Propulsion Research. *Aerospace*, 7(120), 2020.

[6]David Krejci, Lou Grimaud, Tony Schönherr, Valentin Hugonnaud, Alexander Reissner, and Bernhard Seifert. ENPULSION NANO and MICRO propulsion systems: development and testing. In *AIAA Propulsion and Energy Forum*, 2021.

[7]Dillon O'reilly, Georg Herdrich, and Darren F. Kavanagh. Electric propulsion methods for small satellites: A review. *Aerospace*, 8(1):1–30, 2021.

[8]S. N. Bathgate, M. M.M. Bilek, and D. R. McKenzie. Electrodeless plasma thrusters for spacecraft: A review. *Plasma Science and Technology*, 19(8), 2017.

[9] Shunjiro Shinohara. Helicon high-density plasma sources: Physics and applications. *Advances in Physics: X*, 3(1):185–220, 2018.

[10] K. Takahashi. Helicon-type radiofrequency plasma thrusters and magnetic plasma nozzles. In *Reviews of Modern Plasma Physics*, volume 3. Springer Singapore, 2019.

[11] Alfio E Vinci and Stéphane Mazouffre. Direct experimental comparison of krypton and xenon discharge properties in the magnetic nozzle of a helicon plasma source. *Physics of Plasmas*, 28(033504), 2021.

[12] Kazunori Takahashi. Magnetic nozzle radiofrequency plasma thruster approaching twenty percent thruster efficiency. *Scientific Reports*, 11(1):1–12, 2021.

[13] Nicolas Bellomo, Mirko Magarotto, Marco Manente, Fabio Trezzolani, Riccardo Mantellato, Lorenzo Cappellini, Devis Paulon, Antonio Selmo, Davide Scalzi, Marco Minute, Matteo Duzzi, Alessandro Barbato, Alessandro Schiavon, Simone Di Fede, Nabil Souhair, Paola De Carlo, Francesco Barato, Fabiana Milza, Elena Toson, and Daniele Pavarin. Design and In-orbit Demonstration of REGULUS, an Iodine electric propulsion system. *CEAS Space Journal*, (0123456789), 2021.

[14] Seth J Thompson, Fort Collins, Casey C Farnell, Shawn C Farnell, Plasma Controls, Fort Collins, Desiree D Williams, John P Chandler, Fort Collins, John D Williams, and Fort Collins. Evaluation of Iodine Compatible Cathode Configurations. *36th International Electric Propulsion Conference*, pages 1–21, 2019.

[15] M. Light, I. D. Sudit, F. F. Chen, and D. Arnush. Axial propagation of helicon waves. *Physics of Plasmas*, 2(11):4094–4103, 1995.

[16] D. D. Blackwell, T. G. Madziwa, D. Arnush, and F. F. Chen. Evidence for Trivelpiece-Gould Modes in a Helicon Discharge. *Physical Review Letters*, 88(14):4, 2002.

[17] K. Takahashi, T. Lafleur, C. Charles, P. Alexander, R. W. Boswell, M. Perren, R. Laine, S. Pottinger, V. Lappas, T. Harle, and D. Lamprou. Direct thrust measurement of a permanent magnet helicon double layer thruster. *Applied Physics Letters*, 98(14):2–4, 2011.

[18] L. T. Williams and M. L.R. Walker. Thrust measurements of a helicon plasma source. *47th AIAA/ASME/SAE/ASEE Joint Propulsion Conference and Exhibit 2011*, pages 1–15, 2011.

[19] S. Pottinger, V. Lappas, C. Charles, and R. Boswell. Performance characterization of a helicon double layer thruster using direct thrust measurements. *Journal of Physics D: Applied Physics*, 44(23), 2011.

[20] K. Takahashi, C. Charles, R. Boswell, and A. Ando. Performance improvement of a permanent magnet helicon plasma thruster. *Journal of Physics D: Applied Physics*, 46(35), 2013.

[21] Kazunori Takahashi, Yoshinori Takao, and Akira Ando. Thrust imparted by a stepped-diameter magnetic nozzle rf plasma thruster. *Applied Physics Letters*, 113(3), 2018.

[22] J. Navarro-Cavallé, M. Wijnen, P. Fajardo, and E. Ahedo. Experimental characterization of a 1 kW Helicon Plasma Thruster. *Vacuum*, 149:69–73, 2018.

[23] J. Navarro-Cavallé, M. Wijnen, P. Fajardo, E. Ahedo, V. Gomez, A. Giménez, and Mercedes Ruiz. Development and Characterization of the Helicon Plasma Thruster Prototype HPT05M. In *36th International Electric Propulsion Conference*, number September, 2019.

[24] T. A. Collard and B. A. Jorns. Magnetic nozzle efficiency in a low power inductive plasma source. *Plasma Sources Science and Technology*, 28(10), 2019.

[25] Eduardo Ahedo and Jaume Navarro-Cavallé. Helicon thruster plasma modeling: Two-dimensional fluid-dynamics and propulsive performances. *Physics of Plasmas*, 20(4), 2013.

[26] T. Lafleur. Helicon plasma thruster discharge model. *Physics of Plasmas*, 21(4), 2014.

[27] M. Magarotto, D. Melazzi, and D. Pavarin. Study on the influence of the magnetic field geometry on the power deposition in a helicon plasma source. *Journal of Plasma Physics*, 85(4):1–19, 2019.

[28] K. Takahashi, Y. Takao, and A. Ando. Increased Thrust-to-Power Ratio of a Stepped-Diameter Helicon Plasma Thruster with Krypton Propellant. *Journal of Propulsion and Power*, 2020.

[29] J. M. Little and E. Y. Choueiri. Electron Cooling in a Magnetically Expanding Plasma. *Physical Review Letters*, 117(22):1–5, 2016.

[30] T. Lafleur, C. Charles, and R. W. Boswell. Characterization of a helicon plasma source in low diverging magnetic fields. *Journal of Physics D: Applied Physics*, 44(5), 2011.

[31] Alexander Bennet, Christine Charles, and Rod Boswell. Non-local plasma generation in a magnetic nozzle. *Physics of Plasmas*, 26(7), 2019.

[32] I. D. Sudit and F. F. Chen. RF Compensated Probes for High-density Discharges. *Plasma Sources Science and Technology*, 3(2):162–168, 1994.

[33] F. F. Chen. Lectures Notes on Langmuir Probe Diagnostics, 2003.

[34] F. F. Chen. Langmuir probes in RF plasma: Surprising validity of OML theory. *Plasma Sources Science and Technology*, 18(3), 2009.

[35] F. F. Chen. Langmuir probe analysis for high density plasmas. *Physics of Plasmas*, 8(6):3029–3041, 2001.

[36] S. Mazouffre, G Largeau, L Garrigues, C Boniface, and K Dannenmayer. Evaluation of various probe designs for measuring the ion current density in a Hall thruster plume. *35th International Electric Propulsion Conference*, (8-12 October):IEPC–2017–336, 2017.

[37] S. Mazouffre. Mesure de la densité de courant ionique dans le jet plasma d'un propulseur de Hall. Théorie et instrumentation. Technical report, 2016.

[38] S. Mazouffre. Laser-induced fluorescence diagnostics of the cross-field discharge of Hall thrusters. *Plasma Sources Science and Technology*, 22(1), 2012.

[39] A. Lejeune, G. Bourgeois, and S. Mazouffre. Kr II and Xe II axial velocity distribution functions in a cross-field ion source. *Physics of Plasmas*, 19(7), 2012.

[40] A. Kramida, Yu. Ralchenko, J. Reade, and Team NIST ASD. NIST Atomic Spectra Database (ver. 5.8), [Online]. Available: https://physics.nist.gov/asd [2021, June 7]. National Institute of Standards and Technology, Gaithersburg, MD, 2020.

[41] V. Kaufman. Wavelengths and Energy Levels of Neutral Kr^{84} and Level Shifts in All Kr Even Isotopes. *J. Res. Natl. Inst. Stand. Technol.*, 98, 1993.

[42] C. J. Humphreys and E. Paul Jr. Interferometric Observations in the Spectra of ^{86}Kr. *J. Opt. Soc. Am.*, 60:200–205, 1970.

[43] M. Martinez-Sanchez, J. Navarro-Cavallé, and E. Ahedo. Electron cooling and finite potential drop in a magnetized plasma expansion. *Physics of Plasmas*, 22(5):1–12, 2015.

[44] K. Takahashi and A. Ando. Enhancement of axial momentum lost to the radial wall by the upstream magnetic field in a helicon source. *Plasma Physics and Controlled Fusion*, 59(5), 2017.

[45] I. D. Sudit and F. F. Chen. Discharge equilibrium of a helicon plasma. *Plasma Sources Science and Technology*, 5(1):43–53, 1996.

[46] D. Bose, T. R. Govidan, and M. Meyyappan. Modeling of a helicon plasma source. *IEEE TRANSACTIONS ON PLASMA SCIENCE,*, 31(4), 2003.

[47] F. F. Chen and D. Arnush. Generalized theory of helicon waves. I. Normal modes. *Physics of Plasmas*, 4(9):3411–3421, 1997.

[48] P. Chabert and N. Braithwaite. *Physics of Radio-Frequency Plasmas*. Cambridge University Press, 2011.

[49] Yuriko TANIDA, Daisuke KUWAHARA, and Shunjiro SHINOHARA. Spatial Profile of Ion Velocity Distribution Function in Helicon High-Density Plasma by Laser Induced Fluorescence Method. *Transactions of the Japan Society for Aeronautical and Space Sciences, Aerospace Technology Japan*, 14(ists30):$Pb_7 - -Pb_1 2$, 2016.

[50] S. A. Andersen, V. O. Jensen, P. Nielsen, and N. D'Angelo. Continuous supersonic plasma wind tunnel. *Physics of Fluids*, 12(3):557–560, 1969.

[51] E. Ahedo and M. Merino. Two-dimensional supersonic plasma acceleration in a magnetic nozzle. *Physics of Plasmas*, 17(7):1–15, 2010.

[52] M. Merino and E. Ahedo. Plasma detachment in a propulsive magnetic nozzle via ion demagnetization. *Plasma Sources Science and Technology*, 23(3), 2014.

[53] E. Ahedo, S. Correyero, J. Navarro, and M. Merino. Macroscopic and parametric study of a kinetic plasma expansion in a paraxial magnetic nozzle. *Plasma Sources Science and Technology1*, 29(045017):0–20, 2020.

[54] Sara Correyero, Julien Jarrige, Denis Packan, and Eduardo Ahedo. Ion acceleration in the magnetic nozzle of an ECR thruster: Comparison of experimental measurements with a quasi 1D kinetic model. *Space Propulsion 2018*, (May):1–8, 2018.

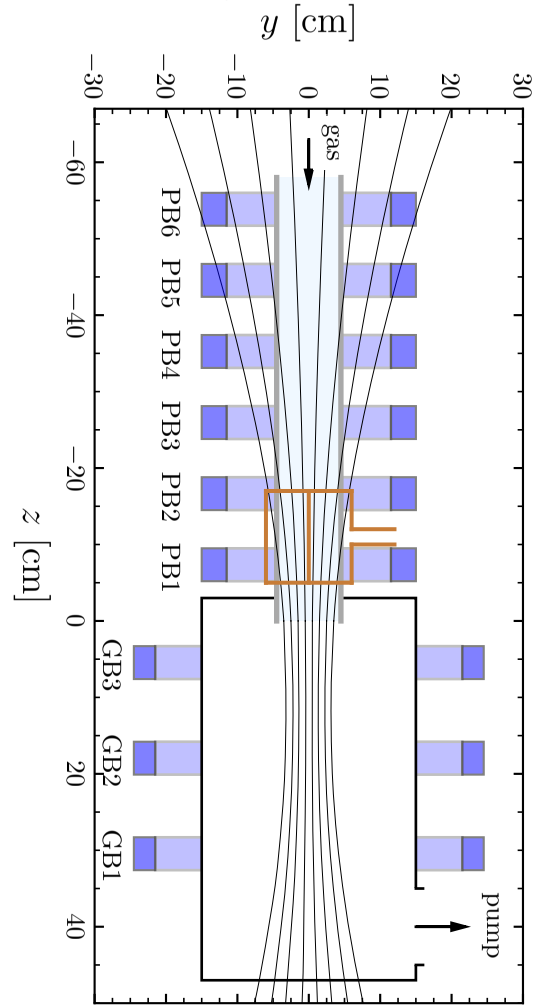

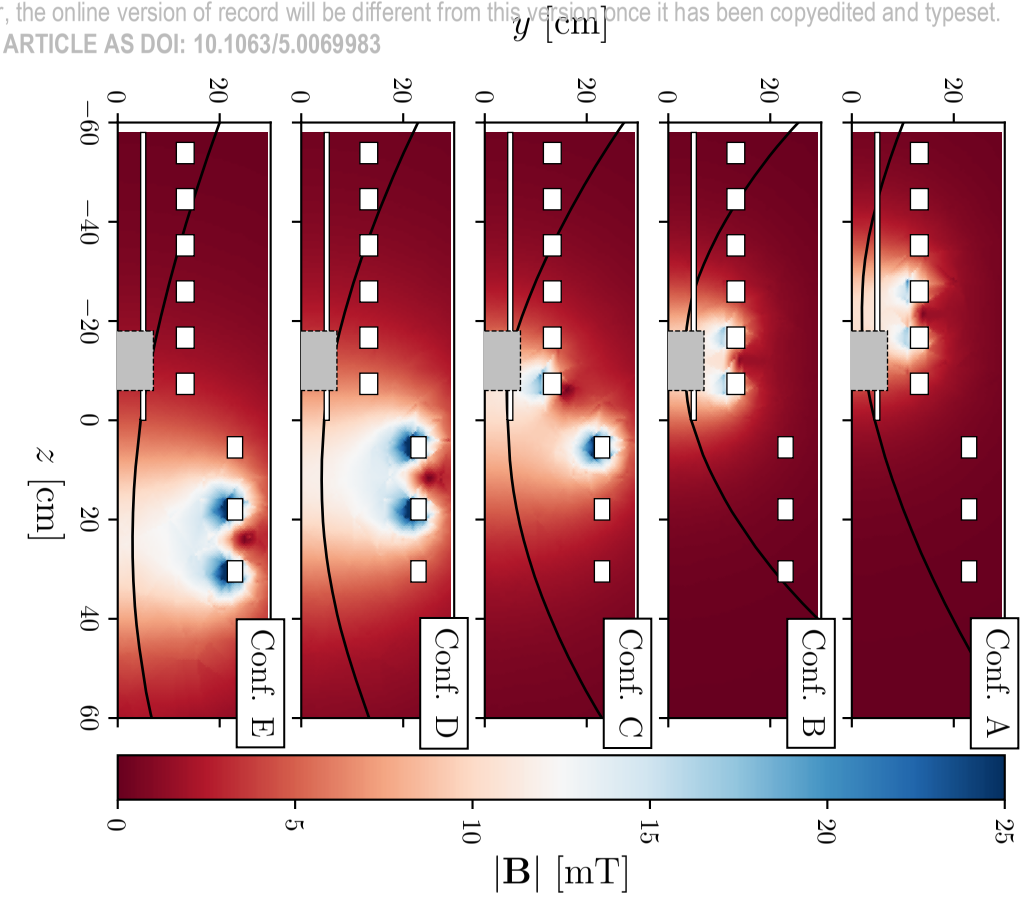

AIP Publishing

Journal of Applied Physics

PLEASE CITE THIS ARTICLE AS DOI: 10.1063/5.0069983

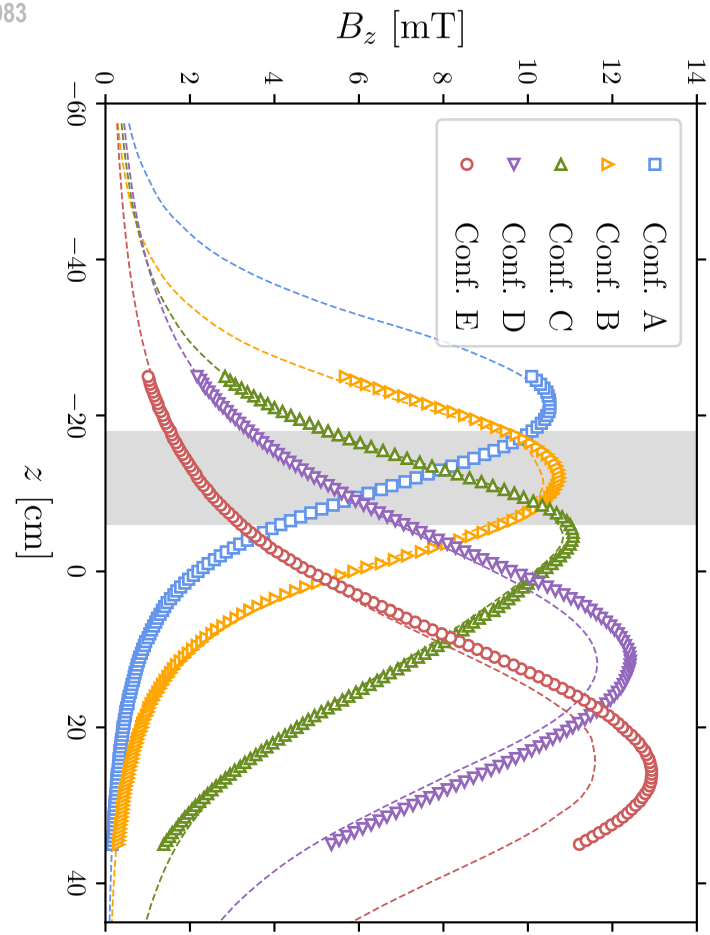

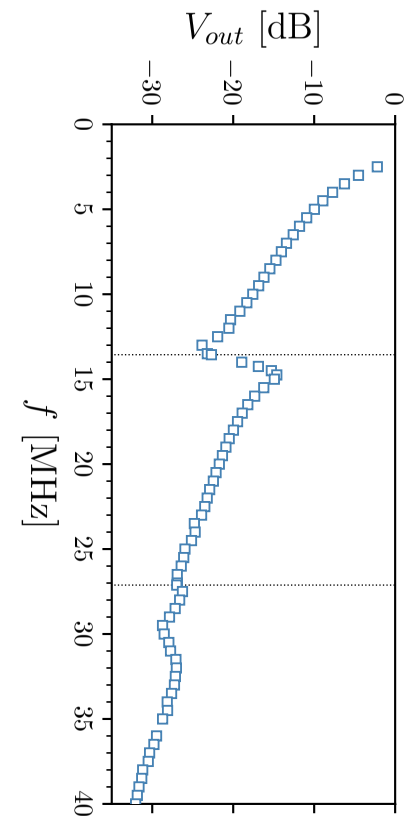

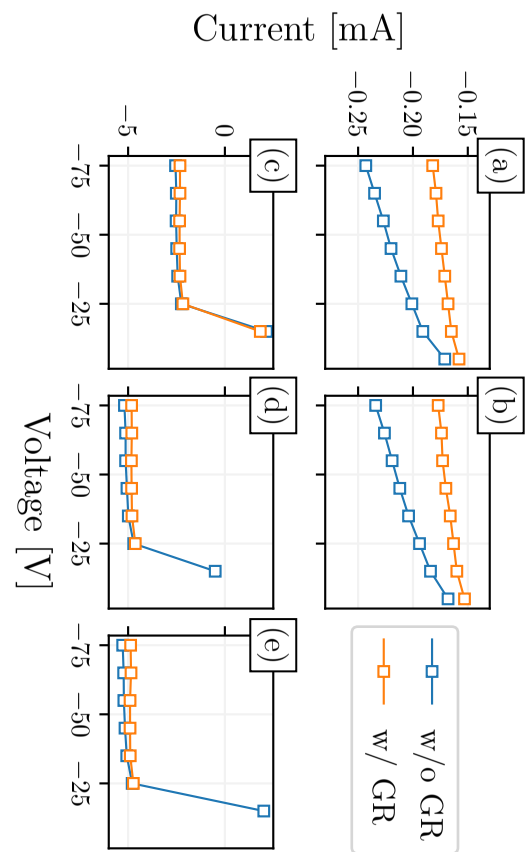

AIP Publishing

Journal of Applied Physics

ACCEPTED MANUSCRIPT

This is the author's peer reviewed, accepted manuscript. However, the online version of record will be different from this version once it has been copyedited and typeset.
PLEASE CITE THIS ARTICLE AS DOI: 10.1063/5.0069983

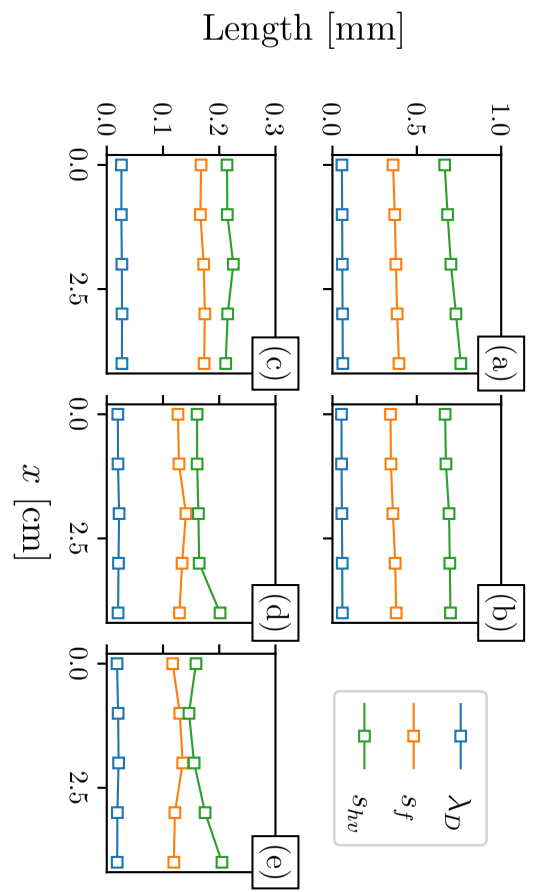

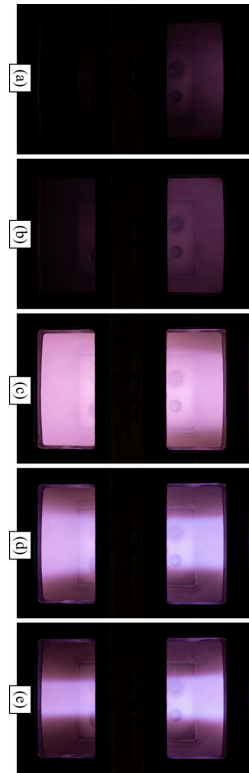

AIP Publishing
Journal of Applied Physics
ACCEPTED MANUSCRIPT

PLEASE CITE THIS ARTICLE AS DOI: 10.1063/5.0069983

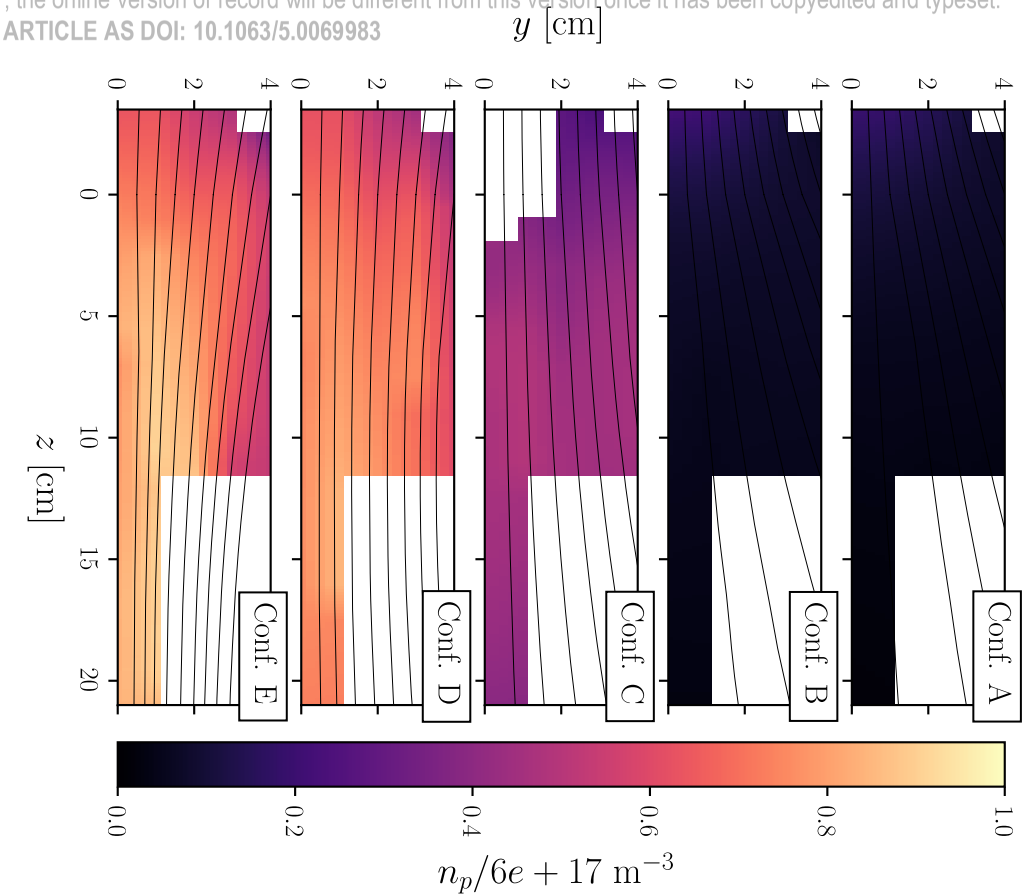

AIP Publishing
Journal of Applied Physics
ACCEPTED MANUSCRIPT

PLEASE CITE THIS ARTICLE AS DOI: 10.1063/5.0069983

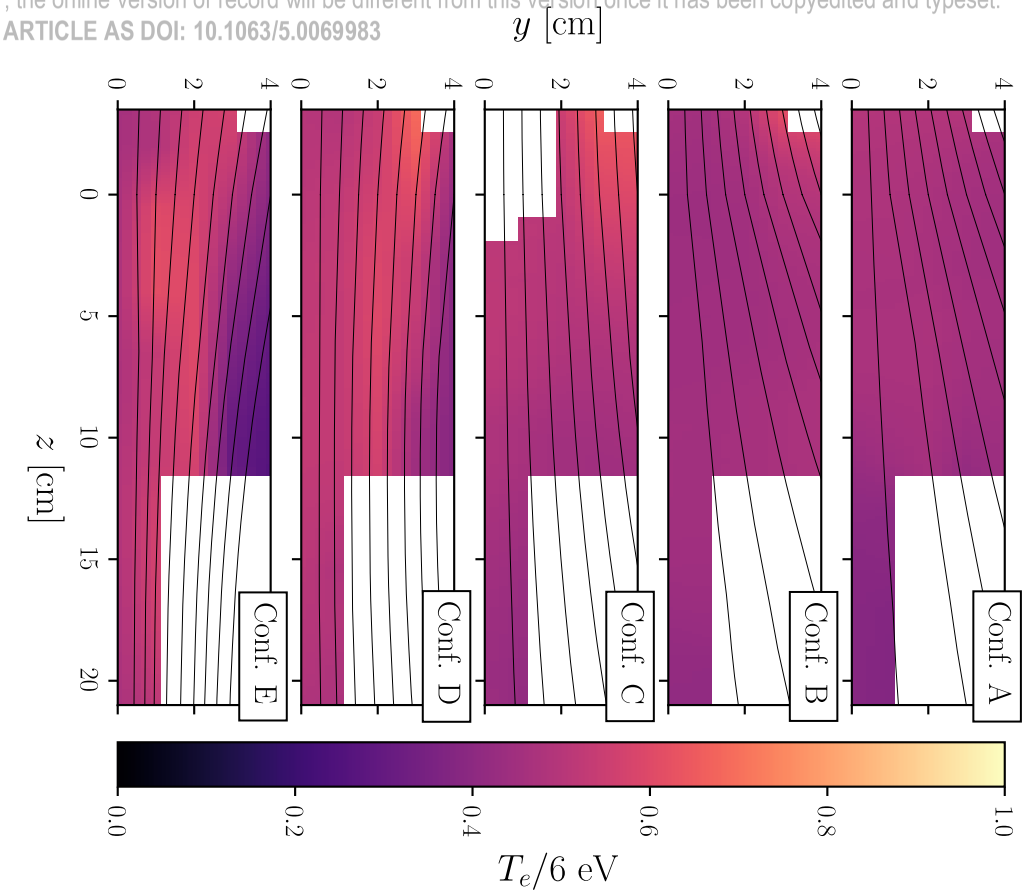

AIP Publishing

Journal of Applied Physics

PLEASE CITE THIS ARTICLE AS DOI: 10.1063/5.0069983

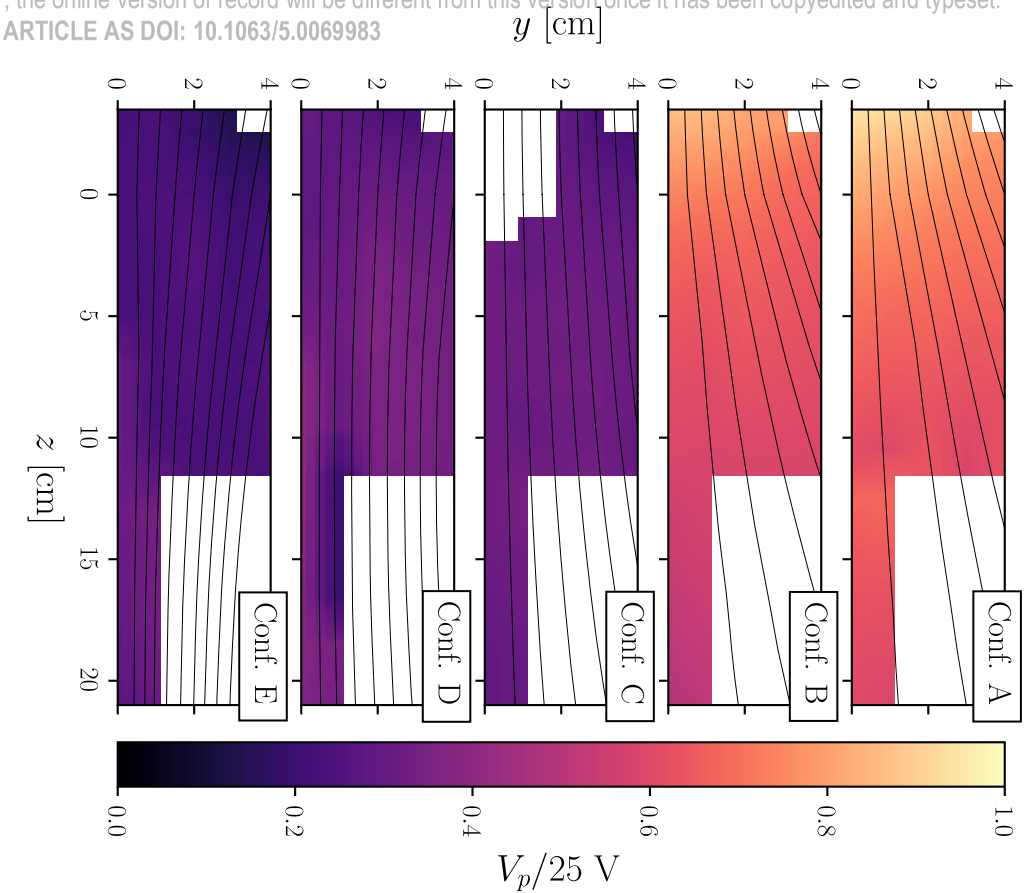

AIP Publishing

Journal of Applied Physics

ACCEPTED MANUSCRIPT

PLEASE CITE THIS ARTICLE AS DOI: 10.1063/5.0069983

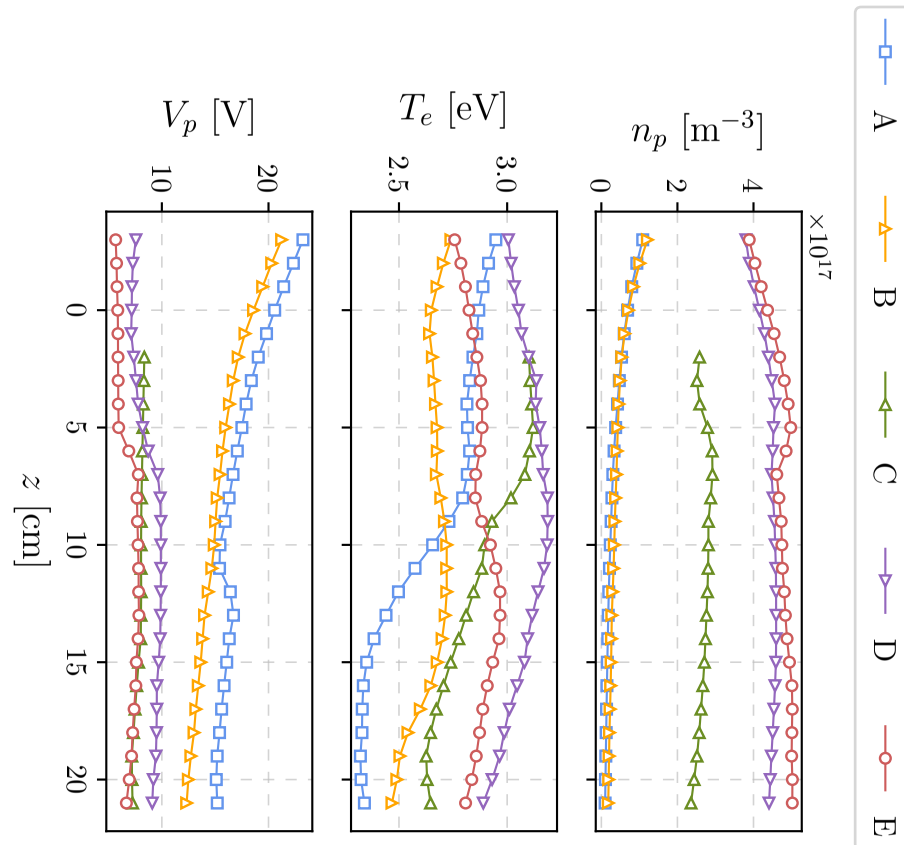

AIP Publishing

Journal of Applied Physics

ACCEPTED MANUSCRIPT

PLEASE CITE THIS ARTICLE AS DOI: 10.1063/5.0069983

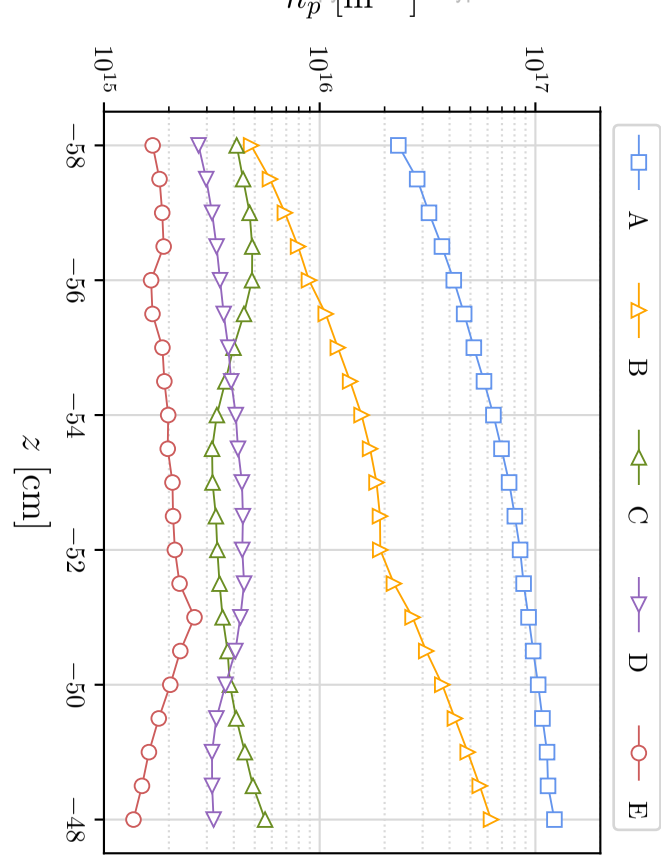

Journal of Applied Physics

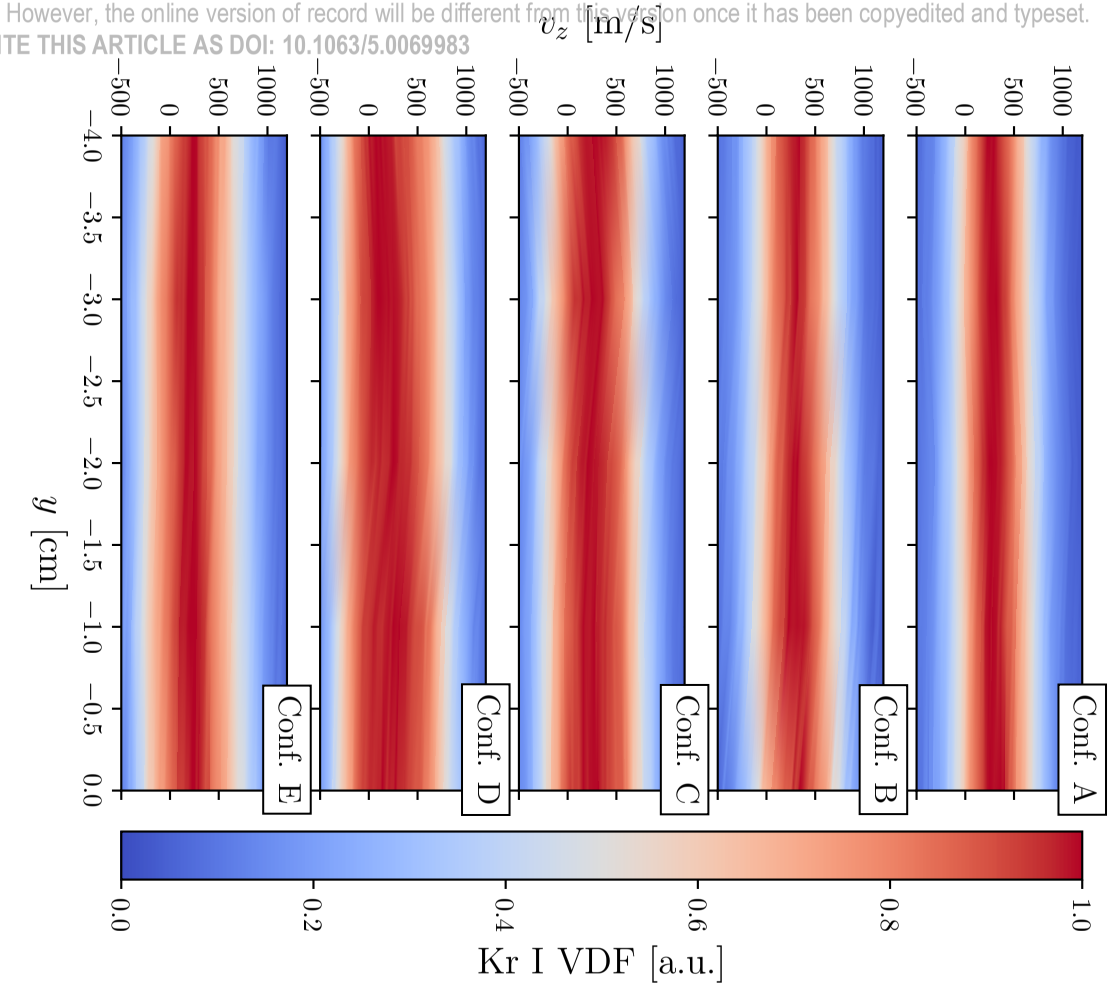

AIP Publishing

Journal of Applied Physics

ACCEPTED MANUSCRIPT

PLEASE CITE THIS ARTICLE AS DOI: 10.1063/5.0069983

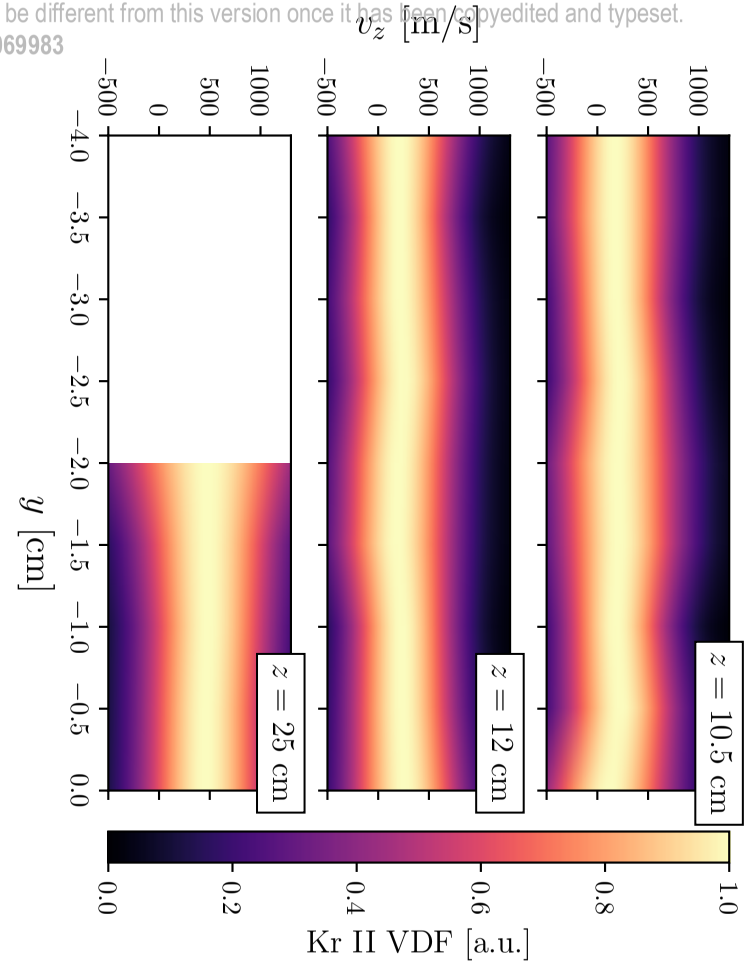

AIP Publishing

Journal of Applied Physics

ACCEPTED MANUSCRIPT

PLEASE CITE THIS ARTICLE AS DOI: 10.1063/5.0069983

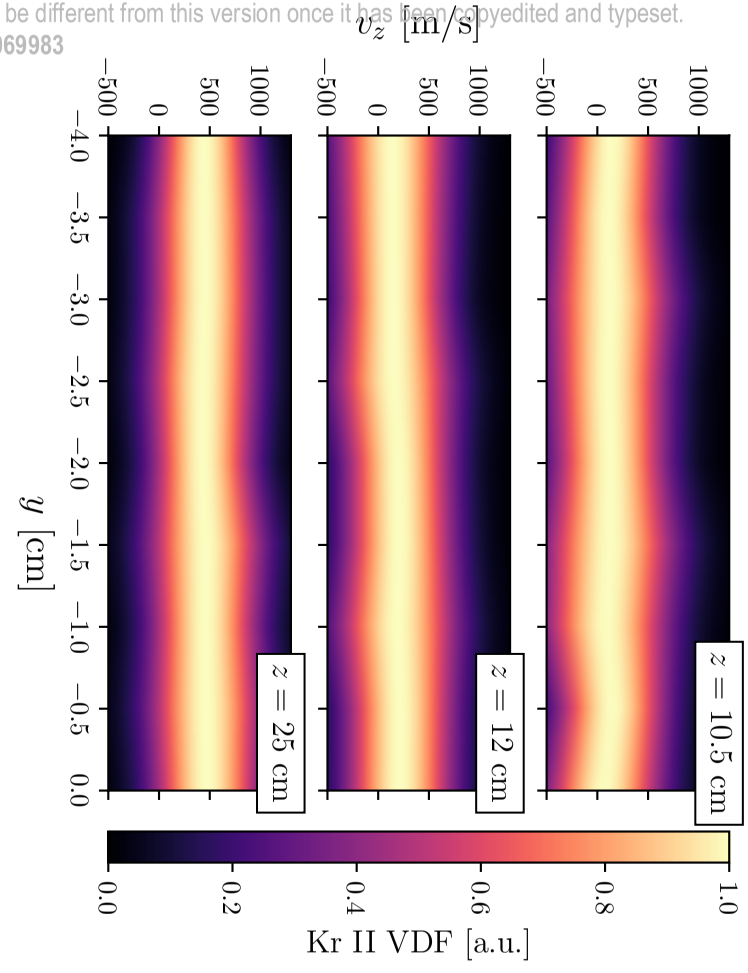

AIP Publishing

Journal of Applied Physics

ACCEPTED MANUSCRIPT

PLEASE CITE THIS ARTICLE AS DOI: 10.1063/5.0069983